

X-RAY ABSORPTION DUE TO COLD GAS IN CLUSTER COOLING CORES

MICHAEL W. WISE

Massachusetts Institute of Technology, Center for Space Research
 Building NE80-6015, Cambridge, MA 02139-4307
 E-mail: wise@space.mit.edu

AND

CRAIG L. SARAZIN

Department of Astronomy, University of Virginia
 P. O. Box 3818, Charlottesville, VA 22903-0818
 E-mail: cls7i@virginia.edu

ABSTRACT

We have calculated the emergent X-ray properties for models of cluster cooling flows including the effects of accumulated cooled material. The opacity of this cooled gas can reduce the overall X-ray luminosity of the cooling flow, and values of \dot{M} based on these luminosities can underestimate the true value by factors of ~ 2 . We find that accumulated cooled material can produce emergent surface brightness profiles much like those observed even for nearly homogeneous gas distributions. Consequently, much more of the gas may be cooling below X-ray emitting temperatures in the central regions of cooling flows ($r \lesssim 10$ kpc) than one would infer from observed X-ray surface brightness profiles assuming the gas was optically thin. Similarly, the central densities and pressures in cooling flows may have been underestimated. We show that distributed absorption in cooling flows produces a number of observable effects in the spectrum which may allow it to be differentiated from absorption due to gas in our Galaxy. These include a characteristic suppression of the continuum below ~ 2 keV, absorption features such as a redshifted O K-edge, and diminished intensity of resonance emission lines. Spectra including the effects of intrinsic absorption are not well fit by foreground absorbing models. Attempting to fit such models to the spatially resolved spectra can lead to underestimates of the true absorbing column by factors of 3–20. Fits to integrated spectra of the entire cooling flow region can either underestimate or overestimate the mass of the absorbing gas depending on the specifics of the model. We discuss the potential detection of these effects with *AXAF*, *XMM*, and *Astro-E*.

Subject headings: cooling flows — galaxies: clusters: general — galaxies: elliptical and lenticular, cD — intergalactic medium — radiative transfer — X-rays: galaxies

1. INTRODUCTION

More than half of the clusters of galaxies observed at X-ray wavelengths exhibit evidence for cool gas in their cores (Edge, Stewart, & Fabian 1992). The cooling time of this gas is often short compared to cluster ages; therefore, the gas cools at rates that are often very large, $\dot{M}_c \sim 10 - 2000 M_\odot \text{ yr}^{-1}$. In the absence of a heating mechanism to balance cooling, gravity and pressure from the hotter, surrounding gas will drive the cooling material into the core of the cluster. If cooling flows are long-lived phenomena, these rates imply that $\sim 10^{12} M_\odot$ of material would cool over the lifetime of the cluster. Determining the final state of this cooling material remains the fundamental problem concerning the cooling flow theory.

The most obvious repositories for the cooling gas are cold molecular and atomic clouds, and stars. The central dominant galaxy in cooling flow clusters often have blue stellar colors in their central regions, which indicate that stars are currently being formed there (McNamara & O’Connell 1992). However, the observed star formation rates are generally $\lesssim 10\%$ of \dot{M}_c . Therefore star formation cannot account for the cooling material without appealing to unusual initial mass functions. Similarly, extensive ef-

forts have been made to detect the accumulated cooled material either as gas at some temperature below the X-ray emitting regime ($T \lesssim 10^6$ K). Gas is seen in cooling flows at 10^4 K (Heckman et al. 1989; Baum 1992) and in a few cases, as neutral atomic or molecular gas (Lazareff et al. 1989; Mirabel, Sanders, & Kazes 1989; McNamara, Bregman, & O’Connell 1990; Jaffe 1992; O’Dea, Baum, & Gallimore 1994a). Dust is also seen in a number of cooling cores (Bregman, McNamara, & O’Connell 1990; Wise et al. 1993). In all cases, however, the detected levels of atomic and molecular gas are too low ($\lesssim 10^9 - 10^{10} M_\odot$) to account for the cooled gas which would accumulate over the age of the cluster.

The detection by White et al. (1991) of excess X-ray absorption in a sample of cluster cooling flows was the first direct evidence for a sufficiently large mass of cold material. Using *Einstein* SSS (Solid State Spectrometer) spectra, these authors found that many cooling flow clusters exhibit significant levels of excess absorption over that expected from the Galaxy with typical excess column densities of 10^{21} cm^{-2} . Evidence for excess absorption in cooling flows has also been found in analyses of X-ray spectra taken with detectors on *Einstein*, *ROSAT*, *BBXRT*, and

ASCA (Lea, Mushotzky, & Holt 1982; Miyaji 1991; Allen et al. 1993; Fabian et al. 1994; Allen & Fabian 1997). The excess absorption columns detected by White et al. (1991) were only observed in clusters with spectral evidence for cooling flows and show some evidence for a correlation between \dot{M} and ΔN_H . This correlation and the observed spatial coincidence between excess absorption and cooling flows suggests that the absorbing material is intrinsic to the cluster and probably located within the cooling flow region. Integrating these excess column densities over the area of the cooling region in cluster cores implies the presence of large quantities of cold absorbing material ($M_{cold} \sim 10^{11} - 10^{12} \dot{M}$) and may represent the first direct evidence for the large amounts of cooled material which current cooling flow models predict (White et al. 1991).

On the other hand, very extensive searches have been made to detect the excess absorber in emission or absorption at radio wavelengths in lines of H I or CO and have not succeeded (e.g., McNamara & Jaffe 1993; Antonucci & Barvainis 1994; O’Dea et al. 1994b). It is becoming difficult to understand how so much X-ray absorbing gas could have escaped detection in other wavebands (e.g., Voit & Donahue 1995).

Often the *ROSAT* PSPC spectra of cooling flows are inconsistent with large columns of excess foreground absorption (e.g., Sarazin, Wise, & Markevitch 1998), but are consistent with and may require large amounts of internal absorption in the cooling flow (Allen & Fabian 1997). For nearby clusters where the *ROSAT* or *ASCA* observations can resolve the cooling flow region, the excess absorption appears to be concentrated to the center of the cluster and cooling flow ($r \lesssim 200$ kpc) (Allen et al. 1993; Irwin & Sarazin 1995; Fabian et al. 1994; Allen & Fabian 1997).

In the standard data analysis of X-ray spectra (e.g., in XSPEC or IRAF/PROS), it is conventional to treat absorbers as lying in the foreground of emission components. This assumption allows the simple arithmetic combination of additive emission sources and multiplicative absorption components. However, X-ray observations suggest that the excess absorbing material in cluster cooling cores occupies the same spatial region as the X-ray emitting gas (Allen et al. 1993; Irwin & Sarazin 1995; Allen & Fabian 1997). Certainly, one would expect such a spatial correlation if the absorber originated as cooling X-ray gas. Including the effects of absorbing material which is intermixed with the X-ray emitting gas is not easily treated within the framework of conventional X-ray spectral modeling. Allen & Fabian (1997) used de-projection techniques based on *ROSAT* PSPC X-ray colors to attempt to determine the three dimensional distribution of the absorption.

In order to provide more accurate models of the X-ray spectra of cooling flows and to assess the effect of intermixed absorbing material, we have calculated the emergent X-ray properties for a set of inhomogeneous cooling flow models including the opacity due to accumulated cooled gas. For a given cooling flow model, we have self-consistently included the X-ray absorption due to varying fractions of the total cooled material generated by the model. The details of the input models and the numerical solution of the radiative transfer equation are described in §2. In §3, we present X-ray luminosities, spectra, integrated surface brightness profiles, and emission line equiv-

alent widths, and spectral profiles for the models. The implications of these results for the interpretation of existing X-ray observations and their application to observations with *AXAF* and *Astro-E* are discussed in §4. In the final section (§5), we summarize our conclusions. We demonstrate that such large quantities of absorbing material can have a significant impact on the observed X-ray properties of cluster cooling flows.

2. CALCULATIONS

2.1. Inhomogeneous Cooling Flow Models

As an input to the transfer calculations, we have selected a number of representative models for inhomogeneous cooling flows, some of which were presented previously in Wise & Sarazin (1993). These models were calculated using the numerical technique described in White & Sarazin (1987) and a subset have been used previously by Sarazin & Graney (1991) to estimate the optical coronal line emission from cooling flows. The optically thin X-ray properties for some of these models have been discussed previously in Wise & Sarazin (1993, hereafter Paper I) while the effects of opacity due to cooling gas were discussed in Wise & Sarazin (1999, hereafter Paper II). We note that the opacity of gas which is in the process of *cooling* below X-ray emitting temperatures (as opposed to the accumulated *cooled* material described in this paper) was shown previously in Paper II to be insufficient to account for the observed excess absorption. These cooling flow models have been discussed in detail in these papers and, in the interest of brevity, we will only briefly describe their relevant characteristics here. For a more detailed discussion, the reader is referred to these sources.

The set of models discussed in Papers I and II span a range of gas deposition including both homogeneous models as well as models with varying levels of inhomogeneity. Homogeneous models, by definition, exhibit a single density and temperature at any given radius. It is important to realize that homogeneous cooling flow models cannot reproduce the observed properties of the excess absorption. In a homogeneous model, all of the gas cools below X-ray emitting temperatures just within the sonic radius, r_s , which is the point where the inflow velocity exceeds the sound speed in the gas (see §2.1 of Paper I and references therein). Values for the sonic radii are typically quite small ($r_s \lesssim 1$ kpc); therefore, any accumulated cooled material would be confined to the very innermost regions of the cooling flow. In contrast, the spectral results of White et al. (1991) indicate that the absorbing material must cover a significant fraction of the cooling flow region ($r \sim 100$ kpc), and the spatially resolved spectral measurements of Allen et al. (1993) and Irwin & Sarazin (1995) confirm this extended absorption. Consequently, in choosing models for these calculations, we have only considered inhomogeneous models which feature cooling material (and by implication *cooled* material) distributed over large spatial scales.

The models used in this paper are listed in Table 1 and assume a spherically symmetric, steady-state inflow with only gravitational and gas pressure forces included. The outer boundary is taken to be the “cooling radius”, r_c , which corresponds to the point at which the instantaneous

isobaric cooling time, t_c , is equal to the age of the cluster. In all cases, the cluster age was taken to be $t_a = 10^{10}$ years. As described in Paper I, the models are completely determined by three quantities: the total inflow rate \dot{M}_c ; the gas temperature T_c ; and the mass deposition profile, $\dot{\rho}(r)$, which describes how inhomogeneous gas cools below X-ray emitting temperatures as a function of radius in the cluster. Both \dot{M}_c and T_c are evaluated at the cooling radius r_c and values of $\dot{M}_c = 100$ or $300 M_\odot \text{ yr}^{-1}$ and $T_c = 8.0 \times 10^7 \text{ K}$ were used for all models.

To specify the mass deposition profile, $\dot{\rho}(r)$, two forms for the mass inflow rate were used. For most of the models, the simple two-phase cooling flow model of White & Sarazin (1987) was employed. In this prescription, the mass deposition profile is parameterized as

$$\dot{\rho}(r) = q \frac{\rho(r)}{t_c(r)} = \frac{2}{5} q \frac{\rho(r)^3 \Lambda[T(r)]}{P(r)} \quad (1)$$

where t_c is the instantaneous isobaric cooling time, $\rho(r)$ is the gas density, $T(r)$ is the gas temperature, and P is the gas pressure. The total emission and cooling rate per unit volume in the gas is $\rho^2 \Lambda(T)$, where Λ is the total emissivity coefficient. The parameter q is referred to as the ‘‘gas loss efficiency parameter.’’ The values of q for each of the models are given in column 5 of Table 1.

In addition to models using the White & Sarazin mass deposition formula (eq. 1), one model was included which used a form for the mass deposition profile derived by various groups from deconvolutions of cluster X-ray surface brightness distributions. Fabian et al. (1984), Stewart et al. (1984), and Thomas et al. (1987) have argued on the basis of these observations that the inflow rate varies as $\dot{M}(r) \propto r$. In the C300_8_fb model, this assumption was adopted, which implies a mass deposition profile of the form

$$\dot{\rho}(r) = \frac{\dot{M}_c}{4\pi r_c r^2}. \quad (2)$$

We note that this model is quite similar to a White & Sarazin model with $q \approx 3.4$.

The various physical parameters for each of the models is given in Table 1. The models use a naming convention of *Cxxx_y_zz*, where *xxx* = \dot{M}_c (in units of $M_\odot \text{ yr}^{-1}$), *y* = T_c (in units of 10^7 K), and *z* = $10 \times q$. For the ‘‘Fabian et al.’’ style model with $\dot{M} \propto r$, *z* = ‘‘fb.’’ Three of the models were presented previously in Sarazin & Graney (1991) and Paper I, and the second column in Table 1 gives their identifications in the nomenclature of those papers. The remaining columns give the cooling rate \dot{M}_c and temperature T_c at the cooling radius, the gas loss parameter, the cooling radius r_c , and the sonic radius r_s . A value of $r_s = 0$ indicates a fully subsonic solution.

2.2. X-Ray Emission

The calculation of the X-ray emission from the gas is discussed in considerable detail in Papers I and II. We included bound-bound, bound-free, free-free, and two-photon emission from ions of the elements H, He, C, N, O, Ne, Mg, Si, S, Ca, Fe, and Ni. Elemental abundances for these species were set at one half of the solar values as defined by Meyer (1979). The emissivities were calculated

under the usual ‘‘coronal limit’’ conditions, as described in Paper I. Of course, the one major exception to these assumptions was the inclusion of the opacity of the gas. We assume that the cooled material is at temperatures below 10^6 K , and produces no appreciable X-ray emission. At the column densities of interest, fluorescent line emission by the cooled gas is not expected to be significant. However, if the columns of cold material in the absorbing clouds were larger, fluorescent emission of Fe K lines might be detectable (Churazov et al. 1998).

2.3. X-Ray Opacity

In calculating the opacity in the cooling flow, we have included contributions from the ambient hot gas, the *cooling* hot gas, and the accumulated *cooled* material. Of these three components, the first two (opacity due to ambient and cooling material) were discussed in detail in Paper II and are treated in the same manner here. Processes contributing to the opacity of the hot gas include resonant line absorption, photoelectric absorption, and electron scattering. As discussed in Paper II, processes such as resonant scattering in the X-ray lines or electron scattering merely redistribute photons within the cluster and produce no net loss in the spatially integrated spectrum. We have also shown previously that the photoelectric opacity in an inhomogeneous cooling flow model due to ambient and cooling intracluster gas is small with $\tau \lesssim 0.01$ (see Paper II). Thus, the opacity from these gas phases cannot account for the observed excess soft X-ray absorption in cooling flows.

In the present paper, we include a new source of opacity associated with the accumulated cooled gas. We assume that this material is relatively cold, so that its opacity is primarily due to photoabsorption. Values for the photoionization cross-sections were taken from an updated version of the Raymond & Smith (1972) emissivity code provided by John Raymond. The opacity of the cooled material will depend somewhat on its ionization state. We have assumed that the cooled material is cold and neutral. Although the physical state of the cooled material has not been established by observations, White et al. (1991), Ferland, Fabian, & Johnstone (1993), and Daines, Fabian, & Thomas (1994) have argued that the absorbing material must be in the form of small, cold clouds to have avoided detection at other wavelengths. As mentioned above, the gas must be at a temperature $\lesssim 10^{6.4}$ for oxygen to retain K-shell electrons and thus present a significant photoelectric cross-section (Shull & Van Steenberg 1982). In fact, the total opacity should remain fairly constant for temperatures much below this value, since the cross-sections are fairly insensitive to changes in the ionization state once the ion has regained a full complement of K-shell electrons.

For a given model, we must also specify the amount and spatial distribution of the cooled material in order to calculate its contribution to the photoelectric opacity. As discussed in §1, our approach is to construct self-consistent models in which the absorbing material is assumed to represent a fraction of all the gas which has cooled below X-ray emitting temperatures over the lifetime of the cooling flow. Thus, we have taken the density of accumulated cold absorbing material as a function of radius in the cluster to

be

$$\rho_{abs}(r) = \eta \dot{\rho}(r) t_a, \quad (3)$$

where $\dot{\rho}(r)$ is the rate at which material is cooling below X-ray emitting temperatures and t_a is the lifetime of the cooling flow, taken here to be 10^{10} years. The factor η is a free parameter which allows us to vary the fraction of the cooling material which is stored as cold absorbing gas. Since it is essentially a deposition efficiency, we assume that $\eta \leq 1$.

Inherent in the adoption of equation (3) is the assumption that the cold material accumulates where it cools. Obviously, this assumption is a simplification, since in practice a cloud of gas which is colder (and thus denser, assuming pressure equilibrium) than the ambient gas will tend to fall in towards the center of the cluster. White & Sarazin (1987) have calculated the distribution of the cooled material assuming it moves on ballistic orbits. Because such material spends a significant fraction of its orbital period at the largest distances from the cluster center, the resulting distributions are reasonably approximated by equation (3). Alternatively, Nulsen (1988) and Fabian et al. (1991) have argued that the cold clouds must comove with the background cooling flow. Such co-motion also results in a distribution similar to equation (3). In any event, the likely departures from equation (3) are in the sense that the profile of the cold gas is more centrally condensed, which would tend to magnify the effects discussed in this paper.

2.4. Numerical Solution of the Transfer Equation

We have solved the transfer of radiation through the cooling flow numerically using the basic algorithm described by Yorke (1980; 1986; 1988). The transfer equation is cast in the cylindrical (b, z) coordinate system of Hummer & Rybicki (1971). Note, we use b rather than p to represent the impact parameter which is fixed for a given ‘‘ray’’ through the flow and corresponds to a given projected radius on the sky. The coordinate z measures the depth into the cluster along each ray. With this choice of coordinates, the transfer equation can be written

$$\frac{dI_E(b, z)}{dz} = \epsilon_E - \kappa_E I_E, \quad (4)$$

where I_E is the intensity of radiation at photon energy E at any point in a given direction along a ray. The emissivity, ϵ_E , contains contributions due to scattering and therefore depends implicitly on integrals of the intensity I_E .

Having specified the variation of ϵ_E and κ_E with radius within the flow, we solve equation (4) using the same numerical code employed in Paper II to calculate the effects of opacity due to the cooling gas. Spherical symmetry and a steady radiation field are assumed. The code is non-relativistic and assumes that velocity v , temperature T , and photon energy E satisfy $|v| \ll c$, $kT \ll m_e c^2$, and $E \ll m_e c^2$. The effects of the flow velocity due to the cooling flow have been included. This code is described in detail in Paper II and Wise (1992). For relevant details of the numerical technique, the reader is referred to these sources.

3. MODEL RESULTS

The models presented here are limited to the cooling flow region of the cluster ($r \leq r_c$). In practice, the cooling flow region is immersed within and smoothly connected to the general intracluster gas which extends out at least another order of magnitude in radius. We have chosen not to include the ambient cluster component to our models in order to focus on the properties of the cooling flow region and avoid introducing additional parameters associated with the cluster distribution. In practice, this decision means that some of the results of our models will differ from the equivalent properties directly observed in real clusters. For example, the X-ray surface brightnesses in our models drop to zero at the cooling radius (e.g., see Figure 2 below). Thus, to compare these profiles with actual cluster surface brightness profiles, the emission due to the foreground and background cluster gas must be removed.

3.1. Total X-Ray Luminosity

Absorption due to the accumulated cold material will diminish the total amount of X-ray emission from the cooling flow. The magnitude of this reduction in the total cooling flow luminosity is shown in Figure 1 as a function of the deposition fraction η . Curves are given for three cooling flow models with a small degree of inhomogeneity $q = 0.1$ (C300.8_01), a moderate degree of inhomogeneity $q = 1.0$ (C300.8_10), and a high degree of inhomogeneity $q = 4.0$ (C300.8_40). Three different bandpasses are presented, corresponding to the total X-ray flux (all photon energies > 0.1 keV), the flux observed with the *ROSAT* PSPC (Position Sensitive Proportional Counter) instrument, and the harder bandpass of the *ASCA* GIS (Gas Imaging Spectrometer). Also shown for comparison are the effects of a column N_H of foreground absorption.

For values of the deposition fraction $\eta \sim 1$, the opacity due to the accumulated cold material can produce a significant reduction in the total X-ray luminosity on the order of 40%, and an even larger reduction in the flux seen in the soft *ROSAT* PSPC bandpass (as large as 60%). The excess absorption columns seen by White et al. (1991) correspond to values of $\eta \approx 0.1$ to 0.4 (see Figure 13 and §4.3 below). We note that these smaller values of η still result in appreciable reductions of $\sim 30\%$ in the total flux and $\sim 45\%$ in the softer *ROSAT* band.

The differences between the three models in Figure 1 are relatively small. At first sight, this lack of distinction is surprising, since a more homogeneous model ($q = 0.1$, C300.8_01) deposits more absorbing material in the center of the cluster where it covers less of the cooling flow region. On the other hand, a more homogeneous model will also produce more of its X-ray emission in this region as well. In fact, equation (3) implies that there is always a correlation between the distribution of the X-ray emissivity of the cooling gas (proportional to $\dot{\rho}$) and the opacity of the absorption due to cooled gas. This correlation decreases the model-to-model differences in the reduction in the X-ray luminosity.

3.2. Emergent X-Ray Spectra

The primary evidence for substantial amounts of cold, absorbing material in the data of White et al. (1991) is a deficit of X-ray emission for photon energies below about 2 keV over that expected from purely galactic absorption. To provide a basis for comparison with spectral observations such as these, we have calculated the emergent X-ray spectra for our models. In Figure 2, the total integrated spectra from 0.1–10 keV are shown for a fairly homogeneous model ($q = 0.1$, C300_8_01) for varying values of η . An absorption component due to foreground Galactic material has not been included in this Figure. As Figure 2 demonstrates, the accumulated cooled material does produce significant absorption below 2 keV even for moderate values of η .

For spatially resolved spectroscopy, the spectral signatures of excess absorption can be even more apparent. Integrated spectra average over the entire range of absorbing column densities in the cooling flow resulting in a lower mean level of absorption. However, a smaller aperture centered on the cluster will average over higher columns resulting in a greater mean absorption. Figure 3 shows several spectra for the same model extracted within a 10 kpc radius circular aperture centered on the core. The degree of absorption is correspondingly greater than in Figure 2.

In addition to the level of soft X-ray absorption, it is also important to note that the accumulated cold material produces a distinctive signature in the *shape* of the emergent spectrum. Absorption due to foreground material produces an exponential fall off in the observed flux toward lower energies since, at a given photon energy E , $f(E) = f_o(E) \exp(-\tau_E)$ where τ_E is the optical depth. However, for absorbing material which is intermixed with the emitting gas, the dependence of the absorption on optical depth is weaker. Roughly, we find that $f(E) \propto f_o(E)/\tau_E$. Consequently for a given absorbing column, foreground absorption will produce deeper absorption edges and a stronger decrease in the spectrum toward lower photon energies than distributed absorption.

This point is illustrated in Figure 4, which compares the spectrum for the $q = 0.1$ (C300_8_01) model with $\eta = 1.0$ (see Figure 2) with the spectrum of the same model with no internal absorption but foreground absorption corresponding to $N_H = 2.5 \times 10^{21} \text{ cm}^{-2}$. This amount of foreground absorption was selected to give roughly the same spectral shape as the internally absorbed model above 1.0 keV. As noted, the model with foreground absorption decreases much more steeply to lower photon energies, and has much deeper absorption edges (e.g., the O K-edge at 0.532 keV). In principle, this difference in the shape of the emergent spectrum may provide a means to distinguish between foreground and intrinsic absorption. For clusters with large foreground Galactic absorption, however, making such a distinction may be problematic (see §4.3).

3.3. X-Ray Surface Brightness Profiles

Centrally peaked X-ray surface brightness profiles represent one of the primary pieces of evidence for the existence of cooling flows in clusters of galaxies. The X-ray emission due to the cooling gas is seen as an excess in the central surface brightness profile relative to that of the outer parts of the cluster (Jones & Forman 1984). In Figure 5, the emergent X-ray surface brightness pro-

files are shown for a fairly homogeneous model ($q = 0.1$, C300_8_01) with values of η ranging from 0 (no absorption) to 1.0 (100% of the accumulated cold material). These profiles correspond to what would be observed in the *ROSAT* PSPC bandpass. Clearly, the central peak in the cooling flow X-ray emission is strongly depressed by the presence of distributed absorption.

For comparison, Figure 5 also shows the X-ray surface brightness profile in the PSPC bandpass for the C300_8_fb model with $\dot{M} \propto r$ and no internal absorption. This model provides a reasonable fit to the observed X-ray surface brightness profiles of many cooling flow clusters (e.g., Fabian et al. 1984). As Figure 5 illustrates, even if only 10% of the cooling material collects in this cold form, substantial reductions in $I_X(b)$ will occur. The rough resemblance of the intrinsically absorbed, essentially homogeneous model profile to that of the optically thin, $\dot{M} \propto r$ model highlights another important consequence of distributed absorption. By suppressing the central peak of the surface brightness profile, a distributed absorber will make a given cluster cooling flow appear more inhomogeneous than it actually is.

ROSAT has provided high quality X-ray surface brightness profiles for many clusters. However, much of the initial work on the X-ray surface brightness profiles of cluster cooling flows was based on observations with the *Einstein* X-ray Observatory (e.g., Fabian et al. 1984). The *Einstein* Observatory had a substantially harder X-ray bandpass, extending to approximately 4 keV. Since the effects of absorption (intrinsic or foreground) are lessened at higher energies, one might expect *Einstein* surface brightness profiles to be less sensitive to the effects of distributed absorption. To test this intuition and provide standards for comparison to the *Einstein* data, we have also calculated the X-ray surface brightness for our models using the response of the *Einstein* IPC (Imaging Proportional Counter). Figure 6 confirms that internal absorption has a smaller effect on I_X as seen by the *Einstein* IPC than *ROSAT*. Roughly speaking, one must increase η by about a factor of two to produce the same effect on *Einstein* observations as with *ROSAT*. The qualitative effect on the surface brightness profile is the same.

3.4. Resonant X-Ray Line Emission

Strong X-ray line emission from cooling gas is one of the characteristic features of cluster cooling flows (Canizares, Markert, & Donahue 1988). Many of the X-ray lines produced by cooling plasma are non-resonance transitions having small oscillator strengths, f , and correspondingly small optical depths due to resonant absorption. Such lines are affected by the internal absorption in the same way as the adjoining continuum discussed above. Consequently, the equivalent widths of optically thin lines are not strongly affected by internal absorption. However, many of the strongest lines arise from resonance transitions and can be moderately optically thick in cooling flows (see Paper II). By itself, resonant line absorption (or scattering) merely redistributes photons spatially and spectrally. When coupled with a significant source of continuum opacity, however, resonant scattering can increase the effects of the absorption on strong, resonance X-ray lines. This increase occurs for lines with significant optical

depth because the effective pathlength through the absorbing medium is increased. We consider some examples of these effects here.

3.4.1. Line Equivalent Widths

To illustrate some of the consequences of intrinsic absorption for emission lines, we consider the observed properties of the Fe XVII $2p^6\ ^1S - 2p^53d\ ^1P^o$ resonance line which has a wavelength of 15.01 Å ($E = 0.826$ keV). This line is produced by gas at temperatures in the range $1\text{--}3 \times 10^6$ K which is cooling rapidly out of the X-ray emitting regime. It has a large oscillator strength ($f = 2.35$) and an optical depth due to resonant absorption of $\tau \sim 0.3\text{--}2.0$ depending on the assumed cooling flow model (see Paper II). Since this Fe XVII line has a low photon energy, it is also particularly susceptible to the effects of internal soft X-ray absorption. In the simulations discussed here, we have assumed the line to be thermally broadened. This assumption maximizes the optical depth in the line. The gas in cluster cores, however, may be quite turbulent ($v_{\text{turb}} \sim 1000$ km s $^{-1}$) which would result in significantly broader emission line profiles and lower line optical depths (see Paper II).

The reduction in the equivalent width, W_η , of the Fe XVII line as a function of η is shown in Figure 7 for several models with varying degrees of inhomogeneity. Models with q values of 0.1, 0.3, 1, and 4 are shown ranging from fairly homogeneous to strongly inhomogeneous, respectively. The model with $\dot{M} \propto r$ is also included for comparison. As Figure 7 shows, resonant soft X-ray lines can be strongly attenuated by internal absorption in cooling flows. For a fixed value of η , the equivalent width of the line decreases (relative to the optically thin value) as the deposition of the cooling material becomes more condensed, i.e. as q decreases. Unlike the total luminosity of the flow, where the spatial coincidence of absorbing and emitting material serve to reduce model-to-model variations, the increase in opacity due to resonant scattering is more sensitive to the location of the absorbing material. Thus, models with differing mass deposition profiles can produce very different reductions in the line fluxes. Note that the reduction in the equivalent width of the line in Figure 7 is in addition to the overall reduction in the emission of continuum and optically thin lines at similar photon energies. Clearly, the fluxes of these lines can be greatly reduced.

3.4.2. Line Surface Brightness Profiles

Like their broadband counterparts, the presence of significant cold, absorbing material will suppress the central peaks in the surface brightness profiles of lower energy X-ray emission lines. Profiles for resonance lines will be particularly affected due to the interplay between absorption from the accumulated cold material and the effects of resonant scattering. Figure 8 shows the emergent equivalent width of the resonance Fe XVII line as a function of projected radius for the fairly homogeneous $q = 0.1$ (C300_8_01) model assuming various values of η . As the amount of internal absorption increases, the gradient in the equivalent width flattens dramatically inside of $r \lesssim 10$ kpc. Again, since the equivalent width compares the flux

in the line to that of the adjoining continuum, the reduction in equivalent width is in addition to the overall reduction in the X-ray surface brightness shown in Figure 5.

In the model without internal absorption ($\eta = 0$), the surface brightness of the line is very strongly concentrated to the center of the cluster. This concentration simply reflects the fact that, for relatively homogeneous models, most of the gas cools inside the sonic radius which occurs at rather small radii (see Paper I). The Fe XVII line is emitted by cooling gas at relatively low temperatures, so the emissivity for this line is very large near the center of the model. Similar results are found for other resonance Fe L lines and for the resonance K-lines of low-Z elements. The K-lines of heavier elements (Si through Ni) are affected less by the opacity of accumulated cooled material due to their higher energy.

3.4.3. Line Spectral Profiles

The combination of continuum opacity from accumulated cooled material and resonance scattering will also alter the spectral line profiles of low-energy resonance lines. The left panel of Figure 9 shows the spectral profile, $\phi_\eta(E)$, of the Fe XVII line in the integrated spectrum of a cooling flow model for different values of the efficiency parameter η . These profiles were calculated for the fairly homogeneous $q = 0.1$ model (C300_8_01) and assume thermal line broadening. The broad wings of the profile for the model without internal absorption are due to gas moving radially inwards at a fairly high velocity near the center of the model (see Paper I).

The right panel highlights the differences in the spectral profile due to optical depth effects and shows the ratio of the profiles with internal absorption to the profile with no accumulated cooled material. Overall, the combined effects of resonance scattering and internal absorption serve to reduce the strength of the line. The broad wings of the line profile are produced by rapidly inflowing gas near the center of the model, where the opacity is largest. Consequently, the wings are reduced more than the line center, where there are contributions from larger radii. For lines produced by emitting material at larger radii or in models with smaller inflow velocities, it is the line center which is most strongly reduced. The spectral profiles depicted in Figure 9 also exhibit asymmetries relative to the line center. These asymmetries arise because blue-shifted photons (due to material flowing into the cluster center on the far side of the cluster) must traverse a greater absorbing column than red-shifted photons (due to material flowing into the cluster center on the near side of the cluster).

Similar results are found for other soft X-ray resonance lines. Emission lines from higher ionization stages such as the Fe K α at 6.7 keV are less effected by photoelectric absorption, although such lines can still be affected by resonance scattering (Paper II). These effects are reduced if the lines are significantly turbulently broadened, as this reduces the line scattering optical depth. In any case, the detection of these effects will require very high spectral resolution observations; as a result, it may be some time before opacity effects on line shapes can actually be observed.

3.5. Absorption Edges

In addition to its broadband effects (see §3.2), accumulated cooled material in the cluster core will produce absorption edges in the emergent X-ray spectra of cooling flows. At the columns of interest here, the strongest spectral feature associated with the absorption is the O K-edge at 0.532 keV (e.g, Figure 4). If the intrinsic absorption is associated with the cooling flow, the O K-edge will be redshifted to lower energies such that $E_{edge} = 0.532/(1+z)$ keV. Thus, two O K-edges will appear in the spectrum: an unredshifted edge due to Galactic gas (and possibly oxygen in the detector and spacecraft environment), and a redshifted edge. Detection of such a redshifted edge feature at the redshift of the cluster would provide definitive evidence that the excess absorbing material was associated with the cooling flow and not due to anomalously high foreground absorption. Arnaud & Mushotzky (1998) have reported detection of such a redshifted O K-edge in the Perseus cluster based on analysis of BBXRT spectra.

We can measure the observed depth of the O K-edge from our self-absorbed cooling flow models directly. In Figure 10, the optical depth in the edge is plotted for a range of deposition efficiencies, η , in the various models. The observed optical depth was determined assuming the decrement in the observed flux at the edge energy was given by $\exp(-\tau_{edge})$. Note that this assumption is equivalent to assuming a foreground absorption model. For $\eta = 1$, the measured depth in the edge ranges between $\tau \sim 0.1$ –0.3 for all the models. Given an absorption cross section at O K of $\sigma \sim 6.0 \times 10^{-22} \text{ cm}^2$, these optical depths imply columns of $\Delta N_H \sim 2$ – $5 \times 10^{20} \text{ cm}^{-2}$ assuming the absorbing material is in the foreground of the cluster. As we show below in §4.3, this “foreground” assumption leads to significant underestimates of the true excess absorbing column. No foreground Galactic column was assumed in Figure 10.

The spatial variation of the O K-edge optical depth is shown in Figure 11. For each model, the cooling region was divided into annular bins 5 kpc wide and the optical depth in the edge was then determined for the spectrum from each bin. The different spatial profiles apparent in Figure 11 simply trace the degree of inhomogeneity, and hence the degree to which the absorbing material is centrally condensed, in the underlying model. For a given model, τ_{edge} increases steadily as one moves to smaller projected radii until the point where the cooling flow becomes optically thick in the edge. In the model with $\dot{M}(r) \propto r$, this point occurs at a radius of ~ 50 kpc; while in the slightly inhomogeneous $q = 0.1$ model, τ_{edge} increases steadily into a radius of ~ 10 kpc. Since this “saturation” point corresponds to the radius at which the actual optical depth in the edge is $\tau \sim 1$, Figure 11 implies that the measured value of τ_{edge} can be used to estimate the true absorbing column at this radius. From Figure 11, the observed values for τ_{edge} at these saturation radii range between ~ 0.25 –0.30 implying underestimates of the true columns by factors of ~ 3 –4. This values are consistent with the results presented below based on spectral fits to the integrated spectra assuming foreground absorption models (see §4.3).

In practice, it is difficult to separate an intrinsic, redshifted O K-edge from a Galactic edge with the *ASCA*

SIS (Solid Imaging Spectrometer) or *AXAF* ACIS (*AXAF* CCD Imaging Spectrometer) because of their spectral resolution at these energies. However, such observations may be possible with *AXAF* for some higher redshift clusters ($z \gtrsim 0.1$), where the intrinsic edge is separated from the Galactic feature by $\gtrsim 50$ eV. Although the High Energy Transmission Grating (HETG) spectrometer on *AXAF* has high spectral resolution, its throughput is low and its resolution is degraded when observing extended sources. Astro-E, on the other hand, should easily be capable of detecting redshifted absorption edge features in cooling flow spectra.

3.6. Scaling of Model Results

Obviously, it is not possible to present results covering the full range of all cluster cooling flow parameters in this study. Thus, we have given a few characteristic examples to demonstrate the effects of internal absorption. However, it is generally possible to crudely assess the effects of internal absorption for other parameter values by approximate scaling of the models presented here. The steady-state models we have presented are primarily characterized by five parameters: the total cooling rate \dot{M}_c ; the temperature at the cooling radius T_c ; the age of the cooling flow t_a ; the gas loss efficiency parameter q ; and the fraction of accumulated cooled gas which is present in an X-ray absorbing form η . In addition, the models depend on the parameters characterizing the gravitational field of the cluster and central galaxy, and the abundances in the cooling gas. However, if the temperature at the cooling radius is sufficiently high and one is not concerned with the details of the innermost parts of the flow near the sonic radius, the hydrodynamical solutions do not depend strongly on the detailed form of the gravitational potential. The atomic physics of the emission processes does depend in a complex fashion on the abundances and the outer temperature, so we will assume these are fixed in the scaling given below.

For a fixed temperature T_c and fixed abundances, the density ρ_c at the cooling radius r_c depends inversely on age, $\rho_c \propto t_a^{-1}$. The total cooling rate in a model scales approximately as $\dot{M}_c \propto \rho_c r_c^3 / t_a$. Thus, the cooling radius in a model with fixed abundances and T_c varies approximately as

$$r_c \propto \dot{M}_c^{1/3} t_a^{2/3}. \quad (5)$$

Equation 3 implies that the total mass of the cold absorber in the model is

$$M_{abs} = \eta \dot{M}_c t_a. \quad (6)$$

Consequently, the column density of the cold absorber $N_H(abs)$ and the implied absorption optical depth τ_{abs} both scale as

$$\tau_{abs} \propto N_H(abs) \propto \frac{M_{abs}}{r_c^2} \propto \eta \dot{M}_c^{1/3} t_a^{-1/3}. \quad (7)$$

Intervening absorption affects the observed properties in nonlinear way; therefore, the value of τ_{abs} must be the same for two models if they are to be scaled to one another.

On the other hand, most of the emission properties of cooling flow models nearly scale with the total cooling rate.

Thus, the luminosity in any spectral feature (and the flux in that feature in the integrated spectrum) approximately scale as

$$L_\nu \propto \dot{M}_c. \quad (8)$$

The surface brightness of most features will scale approximately as

$$I_\nu \propto \frac{L_\nu}{r_c^2} \propto \dot{M}_c^{1/3} t_a^{-4/3}. \quad (9)$$

Resonance emission lines present an exception to these scaling relations (§3.4). The properties of these lines depend on both the optical depth due to absorption by cold material τ_{abs} and due to resonance scattering τ_{rs} . The latter scales approximately as

$$\tau_{rs} \propto \rho_c r_c \propto \dot{M}_c^{1/3} t_a^{-1/3}. \quad (10)$$

Requiring this quantity to be constant would generally make it difficult to scale the models. In what follows, we will consider the scaling of all properties of the models except those associated with resonance emission lines which are optically thick to resonance scattering.

Let us assume one wishes to determine the properties of a model characterized by T_c , q , \dot{M}_c , t_a , and η which is not presented in this paper. Further, assume that a model with the desired T_c and q is presented, but with a different total cooling rate \dot{M}_c^o and age t_a^o . Then, from the grid of models presented in this paper, one should select the model with a value of the deposition efficiency parameter, η^o , given by

$$\eta^o \approx \eta \left(\frac{\dot{M}_c}{\dot{M}_c^o} \right)^{1/3} \left(\frac{t_a}{t_a^o} \right)^{-1/3}. \quad (11)$$

We note that this scaling can break down for models with large values of η and significantly different cooling rates or ages. Strictly speaking, equation 11 could produce values of η^o which are much greater than unity. This much absorption could not be produced by material cooling at the present rate.

Once the value of η^o has been fixed, the luminosity and integrated spectrum of the desired model can be scaled from the corresponding fiducial model using

$$L_\nu \approx L_\nu^o \left(\frac{\dot{M}_c}{\dot{M}_c^o} \right), \quad (12)$$

while the surface brightnesses scale as

$$I_\nu \approx I_\nu^o \left(\frac{\dot{M}_c}{\dot{M}_c^o} \right)^{1/3} \left(\frac{t_a}{t_a^o} \right)^{-4/3}. \quad (13)$$

We have verified these relations for a number of cooling flow models, and find that they work to within 10-20% in essentially all cases.

4. EFFECTS OF INTRINSIC ABSORPTION ON DERIVED QUANTITIES

With the exception of Allen & Fabian (1997), most previous analyses of the X-ray spectra from cluster cooling

flows have not considered the effects of additional absorption due to accumulated cooled material. Traditionally, any absorption in the cooling flow spectra has been assumed to come from foreground material and in many cases has been fixed at the Galactic value as measured by Stark et al. (1992). Neglecting the effects of this material, if present, can lead to serious errors in the derived physical properties of the gas in the cluster core. In the following discussion, we examine the effects of this intermixed internal absorption on a number of physical quantities commonly derived from X-ray observations.

4.1. Total Cooling Rates

Assuming the X-ray luminosity from a cooling flow is due to material cooling isobarically from some temperature T , to first order L_X is simply proportional to the enthalpy of the cooling gas:

$$L_X \approx \frac{5}{2} \frac{kT}{\mu m_p} \dot{M}_c. \quad (14)$$

For a measured total luminosity, L_X , this expression can be inverted to obtain an estimate of the total cooling rate of material. As we demonstrated in §3.1, even moderate amounts of accumulated cooled material can produce significant reductions in the observed X-ray luminosity. Therefore, estimates of the total cooling rate \dot{M}_c based on the *observed* value of L_X will tend to *underestimate* the true value if the effects of internal absorption are neglected. Based on the results in Figure 1, the derived values of \dot{M}_c might be as much as a factor of ~ 2 too low. As we show below (§4.3), estimates of the X-ray cooling rate based on fits to X-ray spectral observations which assume only foreground absorption will tend to underestimate the true absorbing column and therefore \dot{M}_c as well.

Individual X-ray emission lines can also be used to measure the total cooling rate of material in cluster cores. If the line is emitted primarily from material at temperatures below the ambient cluster temperature T_c , then the luminosity in the line is given by

$$L_{line} \approx \frac{5}{2} \dot{M}_c \frac{k}{\mu m_p} \int_0^{T_c} \frac{\Lambda_{line}(T)}{\Lambda(T)} dT, \quad (15)$$

where $\Lambda_{line}(T)$ is the emissivity coefficient of the line. For lines emitted by gas at temperatures which are smaller than T_c , the luminosity is nearly independent of T_c , the details of the cooling, or even the abundances (which affect both $\Lambda_{line}(T)$ and $\Lambda(T)$ in a similar manner). This technique requires high spectral resolution observations and has been applied to a number of clusters based on FPCS data from the *Einstein* X-ray Observatory (Canizares, Markert, & Donahue 1988). The High Energy Transmission Grating (HETG) onboard *AXAF* should also provide data from several cluster cooling cores with sufficient spectral resolution to apply this technique.

For optically thin X-ray emission lines, the effects of intrinsic absorption will reduce the observed luminosity in the line, L_{line} , to the same degree as the nearby continuum. Thus, lines at lower energies will suffer greater attenuation and consequently underestimate the total cooling

rate, \dot{M}_c , to a greater degree relative to lines at higher energies. For example, assuming a value of $\eta \sim 1$, optically thin lines with energies near 0.6 keV could suffer reductions as large as 60% whereas the luminosity of a line at 2.0 keV would be reduced by only 20%. These reductions are in addition to any reduction due to the intervening Galactic absorbing column. The actual observed reductions will of course depend on the true underlying deposition profile of cooling material and the detector response. If the line is a resonance line with an appreciable optical depth, an additional reduction of about a factor of two is possible (see §3.4 and Figure 7).

As an aside, we note that differing amounts of intrinsic absorption in cluster cooling cores may be partially responsible for the scatter observed in correlations between \dot{M}_c and other cooling flow properties. Given the many potential sources of scatter in observed cluster correlations, it seems unlikely that accumulated cold material could be solely responsible. However, as these models illustrate, the magnitude of these effects is such that the presence of this material could represent a significant contribution to the observed scatter in such correlations.

4.2. Spatial Distribution of Cooling Material

Centrally peaked X-ray surface brightness profiles are one of the characteristic features of cluster cooling flows. However, it has been known for some time that the observed profiles are less centrally peaked than would be expected if the gas in cluster cooling flows was homogeneous and all of the gas flowed into the inner regions ($r \lesssim 1$ kpc) before cooling (Thomas et al. 1987; White & Sarazin 1987). The conventional explanation of this discrepancy is that the gas is very inhomogeneous, and that denser lumps of gas cool more quickly. Thus, a significant portion of the gas cools below X-ray emitting temperatures before it flows in very far, and does not contribute to the central X-ray emission. One way of quantifying this model is to calculate the amount of hot gas $\dot{M}(r)$ which is still flowing inward at each radius r . By mass conservation, this quantity is equal to the amount of gas which cools within this radius in steady-state. Thomas et al. (1987) have argued that many clusters are reasonably well represented by a mass deposition profile of the form $\dot{M}(r) \propto r$ out to $r \sim 200$ kpc. One of our models (C300_8_fb) incorporates this spatial variation in the cooling rate.

The implied form of the mass deposition profile $\dot{M}(r)$ will depend on the observed X-ray surface brightness profile $I_X(b)$. However, as discussed in §3.3, intrinsic absorption from accumulated cooled material has the effect of reducing the central surface brightness of cooling flows. Consequently, the gas in cooling flows may be less inhomogeneous than a simple interpretation of the observed surface brightness profiles might imply. This effect is illustrated in Figure 5 which shows the predicted ROSAT PSPC X-ray surface brightness profiles for a slightly inhomogeneous $q = 0.1$ model with different values of η (expressed as percentages). As mentioned previously, cooling flow models with $\dot{M} \propto r$ produce surface brightness profiles in reasonable agreement with X-ray observations. For comparison, the optically thin surface brightness profile for the $\dot{M} \propto r$ model is indicated by the heavy

solid line. Clearly, a value of $\eta \approx 10\%$ is sufficient to bring the surface brightness of this nearly homogeneous $q = 0.1$ model into rough agreement with the optically thin $\dot{M} \propto r$ model. In §4.3 below, we show that this level of internal absorption would correspond to an observed excess column of about $1 \times 10^{21} \text{ cm}^{-2}$ if the spectrum were fit assuming only foreground absorption. This value is similar to the excess columns which have been derived from X-ray spectra of cooling flows under this assumption (White et al. 1991).

As noted above, the variation of the inflow or cooling rate $\dot{M}(r)$ as a function of radius has been used to characterize the degree of inhomogeneity of a cooling flow. We have treated the predicted ROSAT X-ray surface brightness data from our models as observed data, and deprojected the emission to determine $\dot{M}(r)$. Figure 12 shows the deprojected mass deposition profiles corresponding to the ROSAT X-ray surface brightness profiles shown in Figure 5. For comparison, the heavy solid line shows the expected profile for a model with $\dot{M}(r) \propto r$ (C300_8_fb). As the degree of internal absorption is increased ($\eta \rightarrow 1$), the derived $\dot{M}(r)$ profiles steepen which would be interpreted as evidence that more of the gas is cooling below X-ray emitting temperatures at larger radii. Again, a value of $\eta \approx 0.1$ would cause the surface brightness of this fairly homogeneous $q = 0.1$ model to have a mass deposition profile which resembled $\dot{M}(r) \propto r$.

These qualitative results apply to all of the models. We have illustrated the case for the fairly homogeneous $q = 0.1$ model because the effects are particularly striking here. However, we note that the specific values of η required to turn a more centrally condensed mass deposition profile (or equivalently, surface brightness profile) into one which resembles the observed $\dot{M}(r) \propto r$ will depend on the specifics of the input model and the detector response. For example, due to its harder bandpass, if the above comparison were made with *Einstein* IPC data, an η value a factor of two larger would be required to produce the same effect. Similarly, a much smaller spectrally determined excess column of order $3 \times 10^{20} \text{ cm}^{-2}$ would convert a moderately inhomogeneous $q = 1$ model into a $\dot{M}(r) \propto r$ model.

As a final point, we note that the above effects do *not* apply to completely homogeneous models. In such models, the gas does not cool to low temperatures until it is inside the sonic radius which typically occurs at very small radii ($r \lesssim 1$ kpc). Therefore, any intrinsic absorption due to this accumulated cooled material would also be concentrated within a very small region. If present, this material would produce a large reduction in the surface brightness profile but only at the very center of the cluster. It would not affect the surface brightness at larger radii since no absorbing material would have accumulated there.

4.3. Absorbing Columns Estimated from Spectral Fits

The evidence for excess absorption in cluster cooling flows has come mainly from spectral fits such as those by White et al. (1991). As we demonstrated in §3.2, absorbing material intermixed with the emitting plasma produces a characteristic spectral shape in the emergent spectrum which is substantially different from the simple exponential fall-off created by foreground absorption. Consequently,

fits to spectra from self-absorbed cooling flows assuming only foreground absorption will yield erroneous values for the derived columns. Specifically, such fits will tend to *underestimate* the true absorbing column. To quantify this effect, we have fit foreground absorption models to the emergent X-ray spectra of our models with internal absorption. In the following analysis, we have used the effective area and spectral resolution of the *ROSAT* PSPC due to its good soft X-ray response.

4.3.1. Fits to Integrated Spectra

Most observations of excess absorption in cluster cooling flows have been based on the integrated spectra for the entire cooling flow region. For example, the original study by White et al. (1991) utilized the *Einstein* SSS detector with a field of view of 6 arcmin. Most nearby cluster cooling flows are several arcmins in radius which means that the SSS gives the integrated spectrum of the entire cooling flow. Similarly, *ASCA* has a resolution of several arcmins and typically yields integrated spectra for the entire cooling flow region. The *ROSAT* PSPC has a better angular resolution of about 0.5 arcmin, but still only gives a few separate spectra within the cooling flow regions of nearby clusters (e.g., Allen et al. 1993). For comparison to such integrated spectra, we have determined the best-fit foreground column $\Delta N_H(\text{spectral})$ using the equivalent integrated spectra from our models.

To perform the spectral fits, we have used the following procedure. For a given cooling flow model and choice of deposition efficiency, η , we have calculated the integrated, emergent spectrum for the entire cooling flow. This spectrum was then convolved with the instrument response of the *ROSAT* PSPC to obtain the number of “observed” counts per energy bin, F_i^{obs} for this model and choice of η . The instrument response consists of the effective area, $A_{\text{eff}}(E)$, and the redistribution function, $R(E, PHA)$, produced by the PSPC’s finite spectral resolution. As a fitting model, we used the optically thin ($\eta = 0$) spectrum for the selected cooling flow multiplied by varying amounts of foreground absorption and convolved with the PSPC instrument response. For a given choice of N_H , this model yields the expected counts per energy bin, $F_i^{\text{fit}}(N_H)$. The value of N_H which yielded the best fit was then obtained by minimizing the χ^2 statistic

$$\chi^2 = \sum_i \frac{[F_i^{\text{obs}} - F_i^{\text{fit}}(N_H)]^2}{F_i^{\text{fit}}(N_H)}, \quad (16)$$

where i is an index assigned to the spectral energy bins. The F_i^{fit} in the denominator of equation 16 assures the correct behavior if the errors in the observed spectra are dominated by Poisson errors from photon noise. Finally, because all clusters are observed through some amount of Galactic material, both F_i^{obs} and F_i^{fit} were also multiplied by varying amounts of Galactic foreground absorption prior to fitting. Fits assuming Galactic columns of 0.1, 0.2, 1.0, and $2.0 \times 10^{21} \text{ cm}^{-2}$ were calculated and these columns were subtracted from the best-fit foreground absorption values after the fit.

Figure 13 gives the excess column densities determined using the above procedure as a function of the deposition

efficiency η . Using this Figure, we can compare the properties of our models with a given η to the observed properties of clusters for which the excess absorption $\Delta N_H(\text{spectral})$ has been derived. Note that the values in Figure 13 are specific to $\dot{M}_c = 300 M_\odot \text{ yr}^{-1}$ and $t_a = 10^{10} \text{ yr}$. The scaling to other values is given in equation 7. The typical excess columns densities found by White et al. (1991) assuming foreground absorption models are of order $\Delta N_H(\text{spectral}) \approx 1 - 2 \times 10^{21} \text{ cm}^{-2}$. These column values are in the regime where all of the model curves in Figure 13 cross, and correspond to $\eta \approx 0.1$ to 0.4 for all of the models.

Observationally, values of $\Delta N_H(\text{spectral})$ have been used to derive limits on the total amount of cold, X-ray absorbing material in cooling flows. Consequently, it is useful to compare the spectrally derived columns with those actually present. The sense of the difference depends on whether one considers spatially resolved spectra or the integrated spectrum of the entire cooling flow region. For spatially resolved spectra, the spectrally derived column assuming only foreground absorption is always smaller than the actual column along that line of sight. This underestimate occurs because, for intermixed absorption, a fraction of the absorbing material always lies behind a portion of the emitting gas, and thus is not fully effective in producing absorption. However, if one considers the integrated spectrum of an extended region where the absorbing column and emission vary with projected position, the difference can have either sign. A given amount of absorber is more effective if it is concentrated where the emission is most intense, and such a concentration may not be resolved in the integrated spectrum.

The spectrally-derived excess columns in Figure 13 are determined from the integrated spectrum of the entire cooling flow region. Following equation 7, the average column density of hydrogen in our models over the cooling flow region is given by

$$\Delta N_H(\text{true}) = \frac{M_{\text{abs}}}{1.47 m_p \pi r_c^2} = \frac{\eta \dot{M}_c t_a}{1.47 m_p \pi r_c^2}. \quad (17)$$

Figure 14 compares the actual average column densities determined using equation 17 with those derived from fits to the integrated spectrum of the cooling flow region (Fig. 13). The heavy solid line indicates $\Delta N_H(\text{spectral}) = \Delta N_H(\text{true})$. For low column in the inhomogeneous models, the spectrally-derived columns overestimate the real column. For large columns of intrinsic material, $\Delta N_H(\text{true}) \gtrsim 1 \times 10^{21} \text{ cm}^{-2}$, and for the most inhomogeneous models, the spectrally derived column is smaller than the real average column for all of the models by a factor $\lesssim 4$. For the more inhomogeneous models ($q \gtrsim 2$) the measured columns underestimate the true values down to columns of $\Delta N_H(\text{true}) \sim 1-2 \times 10^{20} \text{ cm}^{-2}$.

These results can be compared to a similar analysis performed by Allen & Fabian (1997) for a set of cooling flow clusters observed with the *ROSAT* PSPC. Using XSPEC simulations, these authors have simulated the errors in the apparent excess column for two distributions of internal absorption: a partial covering model and a “multilayer” model which assumes a homogeneous distribution of absorbing throughout the X-ray emitting region. These input models were then fit with a simple uniform foreground

absorption model similar to our procedure. Of the two, this latter model is the closest approximation to the detailed distributions of accumulated cooled material modeled here. For values of $\Delta N_H(\text{true})$ of 1 and $5 \times 10^{21} \text{ cm}^{-2}$ and a Galactic column of $N_H(\text{gal})$ of $1 \times 10^{20} \text{ cm}^{-2}$, these authors find that the fitted column densities underestimate the true “multilayer” columns by factors ~ 4 – 5 . These results are in good agreement with the factors of ~ 3 – 4 obtained from our models. Allen & Fabian (1997) also note that the degree of underestimation is essentially independent of the Galactic column, a result we confirm.

For the more homogeneous models $q \lesssim 2$, the spectrally-derived column can actually over-estimate the true average column for small amounts of absorption. This behavior is seen in Figure 14 for values of $\Delta N_H(\text{true}) \lesssim 5 \times 10^{20} \text{ cm}^{-2}$. In these models, both the emission and absorption are strongly concentrated to the center of the cooling flow. When the emitting and absorbing material are concentrated in this way, a smaller amount of absorber is more effective. One way of understanding this effect is to note that in fairly homogeneous models, the effective radii containing most of the emission and absorption are both much smaller than the cooling radius. Thus, if one averages the absorption over the projected area of the entire cooling flow, as in equation 17, the resulting value of the average column density $\Delta N_H(\text{true})$ will be much smaller than the true value in the region where the absorbing material resides.

4.3.2. Fits to Spatially Resolved Spectra

With the exception of a few nearby clusters observed with *ROSAT*, the cooling cores of clusters have not been well resolved spatially by instruments with good spectral resolution. Consequently, studies of excess absorption have depended primarily on analyses of integrated spectra. However, *AXAF*'s excellent spatial resolution (FWHM ~ 0.5 arcsec) will provide spatially resolved spectra for many cooling flows. With such future data in mind, we have calculated the values of $\Delta N_H(\text{true})$ and $\Delta N_H(\text{spectral})$ as a function of projected radius in the cooling flow. To determine $\Delta N_H(\text{spectral})$, we divided the cooling region into annular bins 5 kpc wide. This choice gives roughly 20 bins over the cooling radius for each model. For a choice of η , the emergent spectra within annular bins was calculated from the model surface brightness using

$$\frac{dL_E}{dE}(b_1 : b_2) = 2\pi \int_{b_1}^{b_2} db' b' I_E(b') \quad (18)$$

where b_1 and b_2 represent the inner and outer radii of the bins. Similarly, emergent spectra were extracted from the corresponding optically thin model for the same set of annuli. These spectra were then fit using the same procedure outlined above to calculate the best-fit values of $\Delta N_H(\text{spectral})$.

For comparison, the true variation of $\Delta N_H(b)$ was calculated directly from the distribution of accumulated cooled

material, $\rho_{abs}(r)$ (see equation 3), using

$$\Delta N_H(b) = \frac{1}{1.47m_p} \int \rho_{abs} dl = \frac{2}{1.47m_p} \int_b^R dr \frac{r \rho_{abs}(r)}{\sqrt{r^2 - b^2}} \quad (19)$$

where l is the distance along the line of sight at a projected radius b . Given $\Delta N_H(b)$, the average column density within an annular bin was then taken to be

$$\langle \Delta N_H \rangle (b_1 : b_2) = \frac{2\pi \int_{b_1}^{b_2} db' b' \Delta N_H(b')}{\pi(b_2^2 - b_1^2)}. \quad (20)$$

We note that equation 20 reduces to equation 17 in the limit that $b_1 \rightarrow 0$ and $b_2 \rightarrow r_c$. These expressions were used to derive the true average column densities for the same annular grid used in determining $\Delta N_H(\text{spectral})$.

Figure 15 shows the results of this spatial analysis for two models: the slightly inhomogeneous $q = 0.1$ model (C300.8_01) and the model with $\dot{M}(r) \propto r$ (C300.8_fb). As expected, the spectrally derived column density underestimates the true column at all projected radii. The magnitude of this error increases as one moves towards the center of the cluster. For the model with $\dot{M}(r) \propto r$, the column determined from spectral fits varies over a range of ~ 3 – 10 as one moves to smaller radii. In the $q = 0.1$ model, more of the absorbing material is concentrated toward the center of the flow producing underestimates of the true absorbing column by factors of ~ 2 – 30 . As before, the Galactic column has been subtracted from the curves in Figure 15. *AXAF*'s spatial resolution should yield spatially resolved spectra, and consequently measurements of ΔN_H , on spatial scales comparable to this example for clusters out to redshifts of $z \sim 0.1$.

5. CONCLUSIONS

In this paper, we have calculated models for the X-ray properties of cooling flow clusters including the effects of opacity due to accumulated cooled material. For consistency, we have assumed that the internal absorber has the same distribution as the gas which is cooling below X-ray emitting temperatures in the models. We have characterized the amount of accumulated absorbing material as a fraction η of the amount of gas which would cool over the lifetime of the cluster ($t_a = 10^{10}$ yr) at the present rates of cooling. The emergent properties of the X-ray emission were then calculated including the effects of radiative transfer through this accumulated material.

The presence of accumulated cooled material will reduce the observed X-ray fluxes and the implied cooling rates of cooling flow clusters below the actual values. Depending on the efficiency with which cooling gas is converted into absorbing material, the fluxes and cooling rates may be underestimated by as much as a factor of two over the 0.1–10 keV energy range. For instruments with softer bandpasses, such as *ROSAT*, the reduction can be higher. Although modeling the effects of the intrinsic absorption with foreground absorption models will reduce the magnitude of this underestimate, these models tend to underestimate the total amount of absorbing material and therefore do not completely compensate for this effect.

Intrinsic absorption produces a characteristic spectral morphology below ~ 2 keV which is not well fit by foreground absorption models. Specifically, internal absorption does not increase in effectiveness as an exponential function of the optical depth, as foreground absorption does. As a result, the integrated X-ray spectra for the models described here do not decline as rapidly at softer energies and the absorption edges are less deep than for models with foreground absorption. For spatially resolved spectra toward the core of the cooling flow, this effect is enhanced. We find that these differences should be discernible in present *ASCA* and future *Astro-E* and *AXAF* spectra. On the other hand, it is difficult to distinguish spectra of models with internal absorption from those with foreground absorption with a partial covering factor.

In addition to its effect on the broadband X-ray spectrum, accumulated cooled material will produce redshifted absorption edges such as the O K-edge at an energy of $0.532/(1+z)$ keV. These redshifted edges provide a direct means of determining whether the absorbing material is intrinsic to the cooling flow and not due to anomalously high foreground absorption. Resolving such redshifted O K-edge features from edges due to foreground material and O in the CCD detectors of *ASCA* and *AXAF* is difficult for nearby clusters given the spectral resolution of these instruments. These features may be detectable in more distant clusters with *AXAF* and *XMM* where the redshifted O K-edge is more cleanly separated or in nearby cooling flows with *Astro-E* which has greater spectral resolution.

The effects of internal absorption can have important implications for the analysis of X-ray surface brightness profiles from cluster cooling flows. Because the absorbing material in our models is concentrated toward the central regions of the cooling flow, it acts particularly to diminish the central peak in the surface brightness and flatten the observed profiles. Starting with *Einstein* observations, it has been noted that cluster cooling flows are less centrally peaked than would be expected if the cooling gas were homogeneous. This fact has led to the canonical view that the gas in cooling flows is rather inhomogeneous and that much of the gas cools at large radii. However, our models indicate that opacity due to accumulated cooled material can produce emergent surface brightness profiles much like those observed even for nearly homogeneous gas distributions ($q = 0.1$). Consequently, much more of the gas may be cooling below X-ray emitting temperature in the central regions of cooling flows ($r \lesssim 10$ kpc) than one would infer from observed X-ray surface brightness profiles assuming the gas was optically thin. Another way of presenting the same result is to note that internal absorption steepens the mass deposition profile, $\dot{M}(r)$, one would derive from the observed surface brightness distribution, making a nearly homogeneous model resemble one with $\dot{M}(r) \propto r$. We note that the reduction in the central surface brightness due to internal absorption would

also mean that central cooling times have been overestimated, and that central gas densities and pressures have been underestimated.

Low energy resonance X-ray emission lines are particularly sensitive to the presence of internal absorption. These lines can have appreciable resonance scattering optical depths in cooling flows, and this scattering enhances the chances of absorption by accumulated cooled material. For lines such as the Fe XVII line at 0.826 keV, the interplay between continuum opacity and resonant scattering can lead to reductions of 20%–80% in the equivalent width of the line. Like their broadband counterparts, estimates of the cooling rate based on such lines will underestimate the true cooling rate. Line surface brightness profiles and spectral profiles are likewise effected. With sufficient spectral resolution, one can resolve distortions in the spectral profiles of these low energy resonance lines due to absorption. However, detection of such signatures requires spectral resolution well beyond that currently available. Our models assume thermal line broadening. If significant turbulence is present in the cooling flow gas, the magnitude of these effects is reduced. Emission lines from high ionization stages, such as the Fe K α line at 6.7 keV, are relatively unaffected by internal absorption though they may still have appreciable resonance scattering optical depths.

Previous studies of intrinsic absorption in cooling flows have primarily determined the amount of absorbing material by fitting foreground absorption models to the observed X-ray spectra. As our models indicate, the spectral signatures of accumulated cooled material are not well fit by such models. For spatially resolved spectra, the spectrally derived columns always underestimate the actual columns along the line of sight, typically by a factor of ~ 3 –20 depending on the specifics of the cooling flow model. If the amount of excess absorption is derived from integrated X-ray spectra for the entire cooling flow (as has generally been the case to date due to the limited spatial resolution of the spectrometers used), the situation is more complicated. For large columns or fairly inhomogeneous models, the absorption is always underestimated this way. However, for small columns in nearly homogeneous models, the degree of excess absorption can be overestimated. This effect occurs because both the emission and absorption in nearly homogeneous models is strongly centrally concentrated, and a small amount of absorbing material is more effective in this case.

C. L. Sarazin would like to thank A. Fabian for helpful conversations. C. L. Sarazin was supported in part by NASA Astrophysical Theory Program grant NAG 5-3057. M. Wise's research at M.I.T. is supported in part by the *AXAF* Science Center as part of Smithsonian Astrophysical Observatory contract SVI-61010 under NASA Marshall Space Flight Center.

REFERENCES

- Allen, S. W., Fabian, A. C., Johnstone, R. M., White, D. A., Daines, S. J., Edge, A. C., & Stewart, G. C. 1993, *MNRAS*, 262, 901
 Allen, S. W., & Fabian, A. C. 1997, *MNRAS*, 286, 583
 Antonucci, R., & Barvainis, R. 1994, *AJ*, 107, 448
 Arnaud, K. A., & Mushotzky, R. F. 1998, *ApJ*, 501, 119
 Baum, S. A. 1992, in *Clusters and Superclusters of Galaxies*, ed. A. C. Fabian, (Dordrecht: Kluwer), 171
 Bregman, J. N., McNamara, B. R., & O'Connell, R. W. 1990, *ApJ*, 351, 406
 Canizares, C. R., Markert, T. H., & Donahue, M. E. 1988, in *Cooling Flows in Clusters and Galaxies*, ed. A. C. Fabian (Dordrecht: Kluwer), 63

- Daines, S. J., Fabian, A. C., & Thomas, P. A. 1994, MNRAS, 268, 1060
- Edge, A. C., Stewart, G. C., & Fabian, A. C. 1992, MNRAS, 258, 177
- Fabian, A. C. 1994, AR&AA, 32, 277
- Fabian, A. C., Arnaud, K. A., Bautz, M. W., & Tawara, Y. 1994, ApJ, 436, L63
- Fabian, A. C., Nulsen, P. E. J., & Canizares, C. R. 1984, Nature, 310, 733
- Fabian, A. C., Nulsen, P. E. J., & Canizares, C. R. 1991, A&AR, 2, 191
- Ferland, G. J., Fabian, A. C., & Johnstone, R. M. 1994, MNRAS, 266, 399
- Heckman, T. M., Baum, S. A., van Breugel, W. J., & McCarthy, P. 1989, ApJ, 338, 48
- Hummer, D. H., & Rybicki, G. B. 1971, MNRAS, 152, 1
- Irwin, J. A., & Sarazin, C. L. 1995, ApJ, 455, 497
- Jaffe, W. 1992, in Clusters and Superclusters of Galaxies, ed. A. C. Fabian (Dordrecht: Kluwer), 109
- Jones, C., & Forman, W. 1984, ApJ, 276, 38
- Lazareff, B., Castets, A., Kim, D.-W., & Jura, M. 1989, ApJ, 336, L13
- Lea, S. M., Mushotzky, R. F., & Holt, S. S. 1982, ApJ, 262, 24
- Matilsky, T., Jones, C., & Forman, W. 1985, ApJ, 291, 621
- McNamara, B. R., Bregman, J. N., & O'Connell, R. W. 1990, ApJ, 360, 20
- McNamara, B. R., & Jaffe, W., 1993, A&A, 282, 673
- McNamara, B. R., & O'Connell, R. W. 1992, ApJ, 393, 579
- Meyer, J-P. 1979, Les Elements et leurs Isotopes dans l'Univers, Comm. 22 Liège Ap. Symp., 153
- Mirabel, I. F., Sanders, D. B., & Kazes, I. 1989, ApJ, 340, L9
- Miyaji, T. 1991, BAAS, 23, 1336
- Nulsen, P. E. J. 1988, in Cooling Flows in Clusters and Galaxies, ed. A. C. Fabian (Dordrecht: Kluwer), 175
- O'Dea, C. P., Baum, S. A., & Gallimore, J. F. 1994a, ApJ, 436, 669
- O'Dea, C. P., Baum, S. A., Maloney, P. R., Tacconi, L. S., & Sparks, W. B. 1994b, ApJ, 422, 467
- Raymond, J. C. & Smith, B. W. 1977, ApJS, 35, 419
- Sarazin, C. L. 1988, X-ray Emission from Clusters of Galaxies (Cambridge: Cambridge Univ. Press)
- Sarazin, C. L., & Graney, C. M. 1991, ApJ, 375, 532
- Sarazin, C. L., Wise, M. W., & Markevitch, M. 1998, ApJ, 498, 606
- Shull, J. M., & Van Steenberg, M. 1982, ApJS, 48, 95
- Stark, A. A., Gammie, C. F., Wilson, R. W., Bally, J., Linke, R. A., Heiles, C., & Hurwitz, M. 1992, ApJS, 79, 77
- Stewart, G. C., Fabian, A. C., Jones, C., & Forman, W. 1984, ApJ, 285, 1
- Thomas, P. A., Fabian, A. C., & Nulsen, P. E. J. 1987, MNRAS, 228, 973
- Voit, G. M., & Donahue, M. 1995, ApJ, 452, 164
- White, D. A., Fabian, A. C., Johnstone, R. M., Mushotzky, R. F., & Arnaud, K. A. 1991, MNRAS, 252, 72
- White, R. E., & Sarazin, C. L. 1987, ApJ, 318, 621
- Wise, M. W. 1992, Ph.D. thesis, University of Virginia
- Wise, M. W., O'Connell, R. W., Bregman, J. N., & Roberts, M. S. 1993, ApJ, 405, 94
- Wise, M. W. & Sarazin, C. L. 1993, ApJ, 415, 58 (Paper I)
- Wise, M. W. & Sarazin, C. L. 1999, in preparation (Paper II)
- Yorke, H. W. 1980, A&A, 86, 286
- Yorke, H. W. 1986, in Astrophysical Radiation Hydrodynamics, ed. K.-H. Winkler & M. L. Norman (Dordrecht: Reidel), 141
- Yorke, H. W. 1988, in Radiation in Moving Gaseous Media, ed. Y. Chmielewski & T. Lanz (Geneva: Geneva Obs.), 193

Table 1:

Cluster Cooling Flow Models						
Model	Previous Model	\dot{M}_c ($M_\odot \text{ yr}^{-1}$)	T_c (K)	Gas Loss	r_c (kpc)	r_s (pc)
C300_8_01		300	8.0×10^7	$q = 0.1$	95.6	582
C300_8_03		300	8.0×10^7	$q = 0.3$	93.5	414
C300_8_10	C3	300	8.0×10^7	$q = 1.0$	87.6	115
C300_8_40	C4	300	8.0×10^7	$q = 4.0$	72.3	0
C300_8_fb	C5	300	8.0×10^7	$\dot{M} \propto r$	83.7	11
C100_8_10		100	8.0×10^7	$q = 1.0$	61.3	69

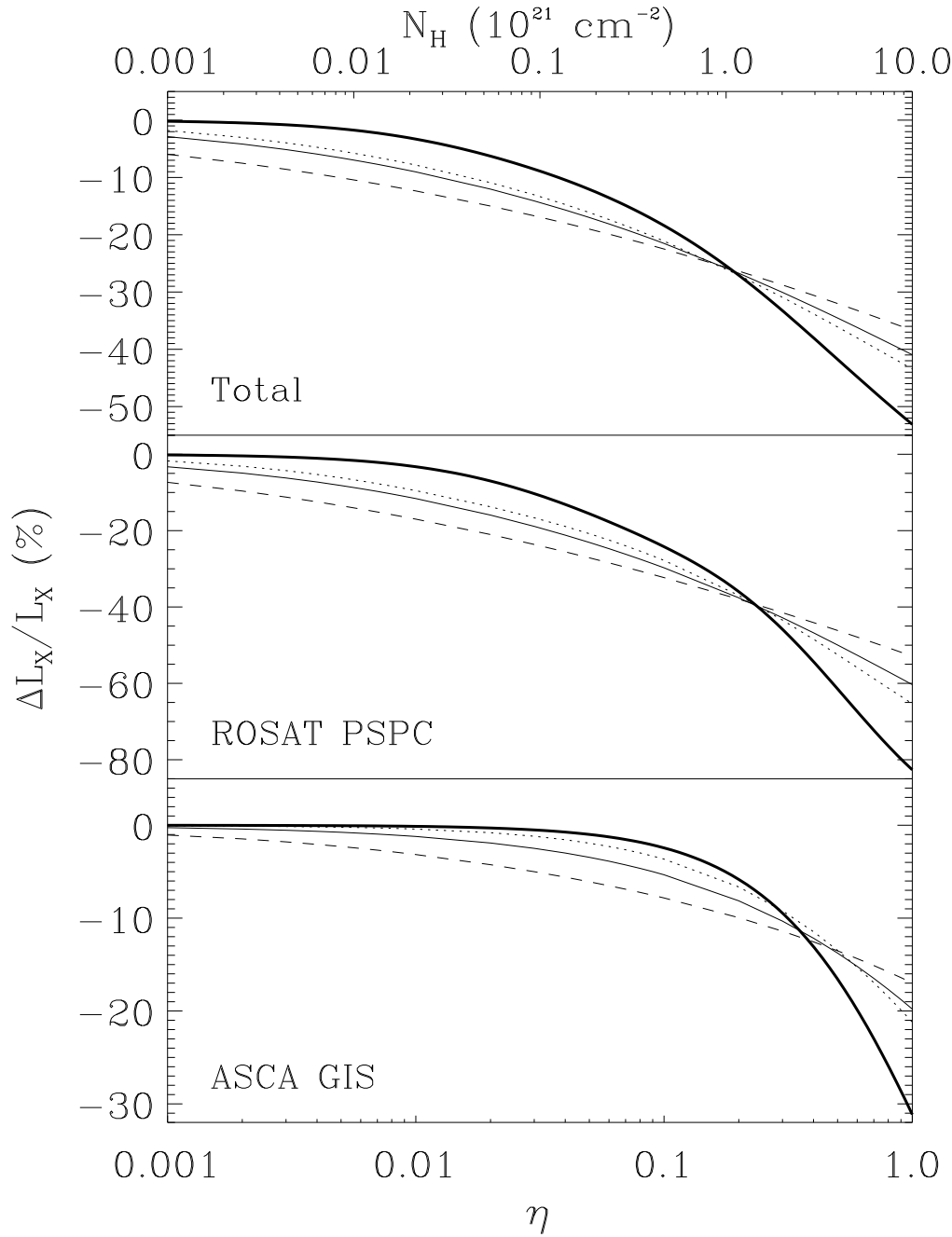


Fig. 1.— The percentage reduction in the X-ray luminosity as a function of the efficiency parameter η . The top panel corresponds to the total luminosity from 0.1–10 keV. The middle and bottom panels show the reduction in the *ROSAT* PSPC and *ASCA* GIS bandpasses, respectively. In the three panels, curves are shown for several different inhomogeneous models considered in the text. The solid line corresponds to a model with a moderate q value of 1.0 while the dashed and dotted lines correspond to the extremes of the model grid. The dashed curve shows the reduction for a model with $q = 0.1$ while the dotted line shows a model with $q = 4.0$. The heavy solid line in each panel indicates the percentage reduction in the various luminosities for a simple foreground absorption model with varying column densities N_H . The abscissa for the foreground absorption curves is indicated along the top axis of the plot.

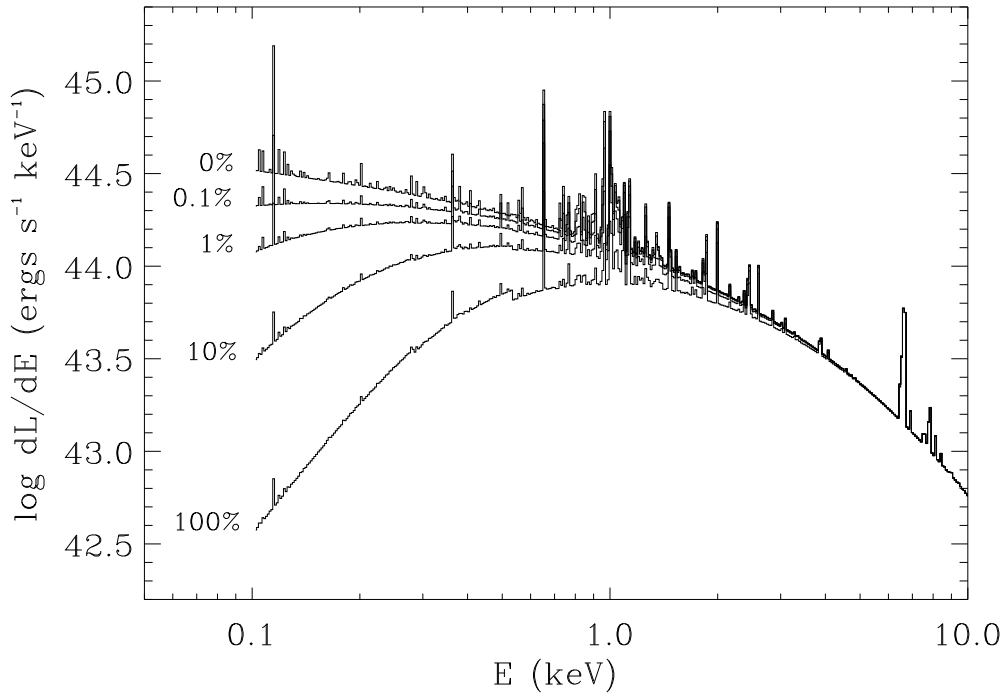


Fig. 2.— Total integrated X-ray spectra as a function of photon energy for the $q = 0.1$ (C300_8_01) model. Curves are shown for differing values of the efficiency parameter, η , described in the text. A value of $\eta = 0$ corresponds to the optically thin case. Each curve is labeled with the corresponding value of η .

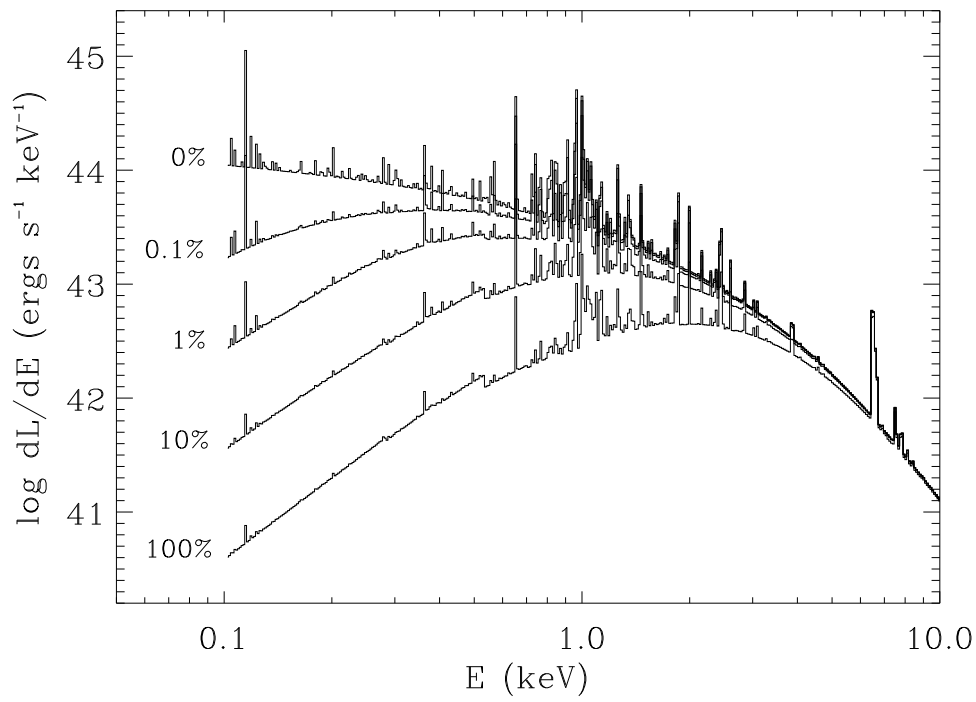


Fig. 3.— The central X-ray spectra as a function of photon energy for the $q = 0.1$ (C300.8_01) models. This is the spectrum from a central circular aperture with a projected radius of 10 kpc. The notation is the same as Figure 2.

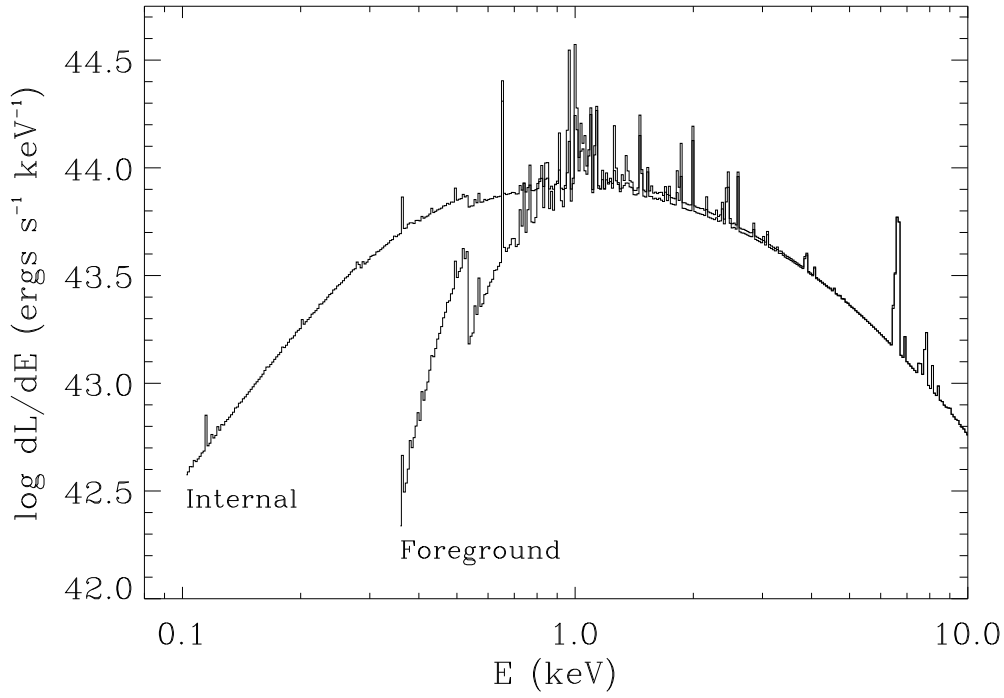


Fig. 4.— The emergent X-ray spectrum from the $q = 0.1$ (C300_8_01) model with intrinsic absorption given by $\eta = 1$ is compared to the same cooling flow model with no internal absorption, but with a foreground absorption of $N_H = 2.5 \times 10^{21} \text{ cm}^{-2}$. Note that these spectra have similar shapes near 1 keV, but the foreground absorption model falls off more rapidly at lower photon energies.

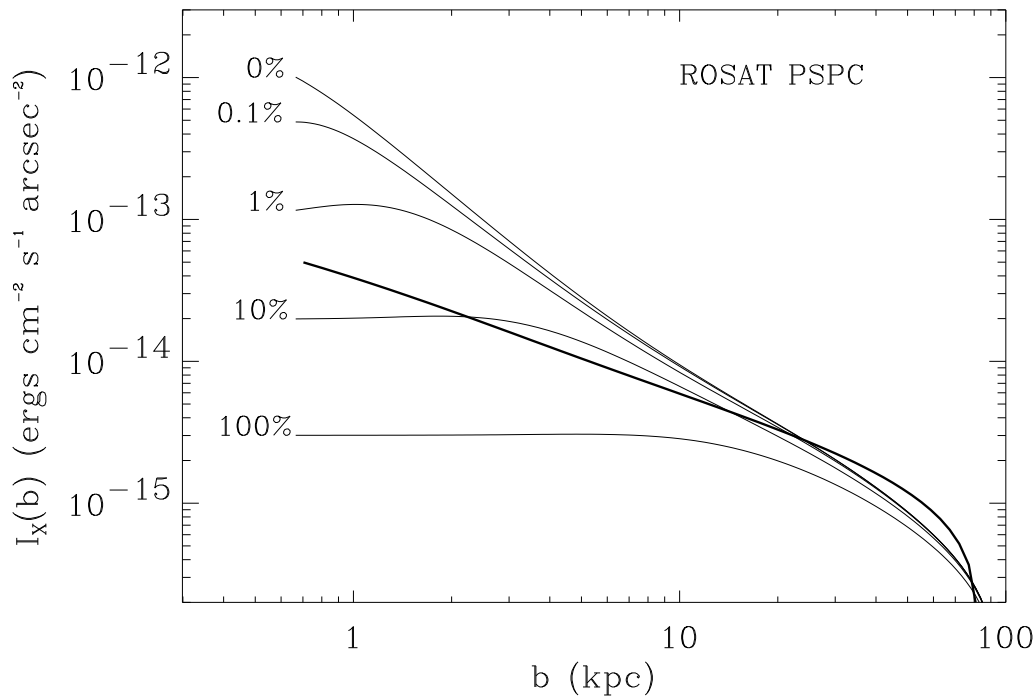


Fig. 5.— The emergent X-ray surface brightness profile in the *ROSAT* PSPC bandpass as a function of projected radius for different values of the efficiency parameter, η . Curves are shown for the nearly homogeneous $q = 0.1$ model and $\eta = 0$ corresponds to the optically thin surface brightness profile. The heavy solid line represents the expected surface brightness profile for a model with $\dot{M}(<r) \propto r$. Each curve is labeled with the corresponding deposition efficiency η expressed as a percentage.

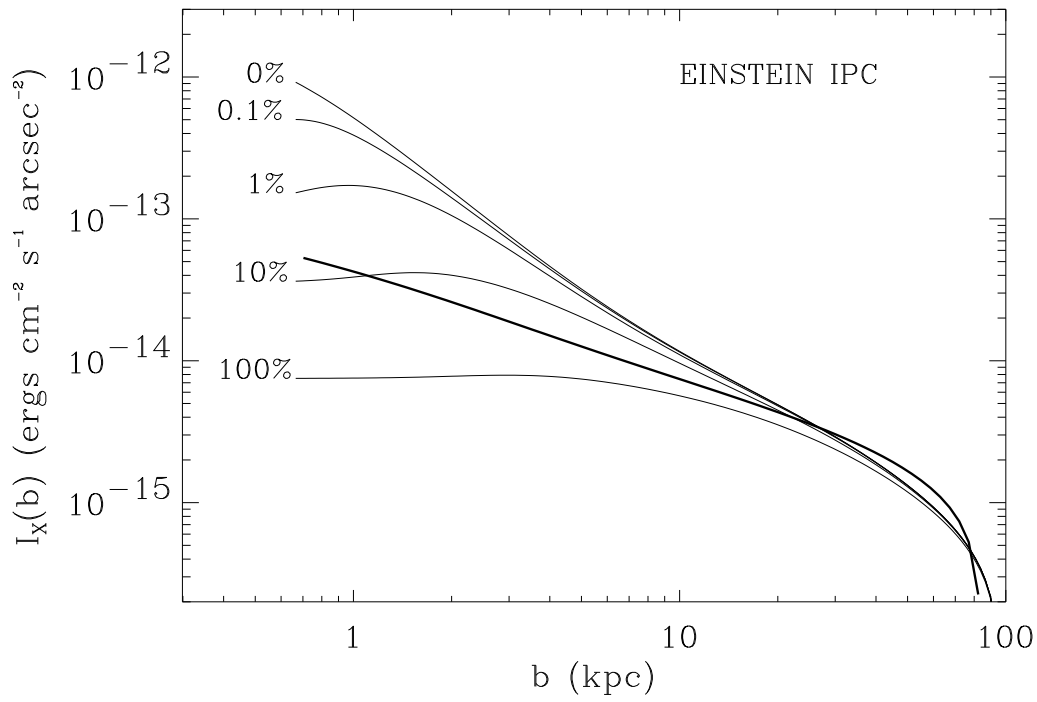


Fig. 6.— The emergent X-ray surface brightness profile as measured in the harder *Einstein* IPC bandpass. The notation is the same as Figure 5.

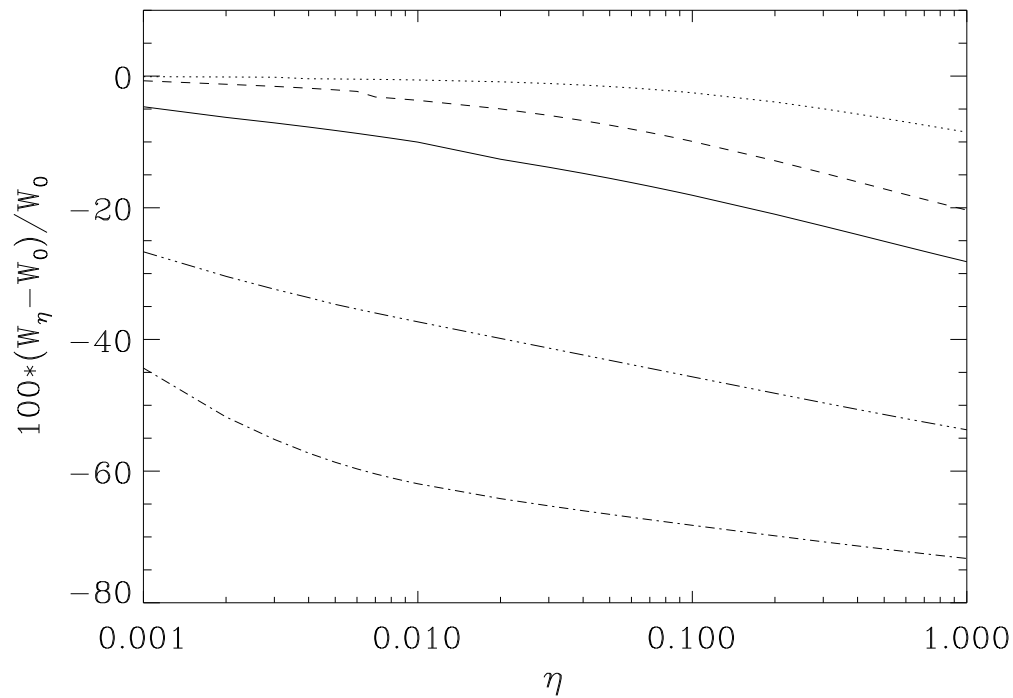


Fig. 7.— The percentage reduction in the total equivalent width, W_η , of the resonance Fe XVII line at 0.826 keV as a function of the deposition efficiency η discussed in the text. Reductions are calculated relative to the optically thin equivalent width, W_o , for that model. Curves are shown for varying values of q : $q = 0.1$ (C300_8_01, dash-dot line), $q = 0.3$ (C300_8_03, dash-dot-dot-dot line), $q = 1.0$ (C300_8_10, solid line), and $q = 4.0$ (C300_8_40, dotted line). The reduction for a model with $\dot{M} \propto r$ is also included for comparison (C300_8_fb, dashed line).

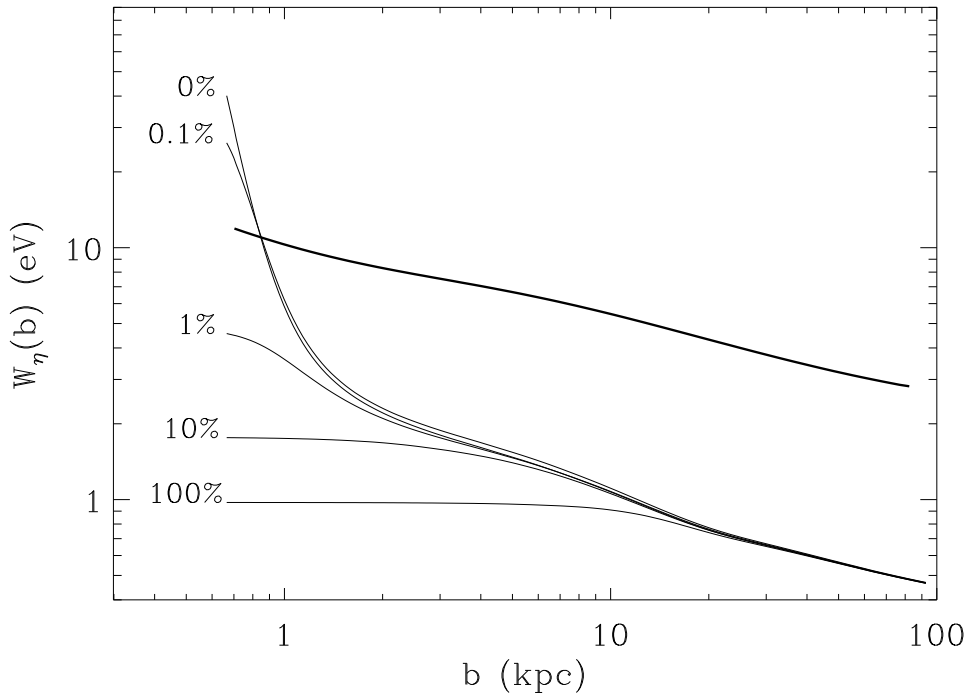


Fig. 8.— The equivalent width, W_η , of the resonance Fe XVII line at 0.826 keV as a function of projected radius for the fairly homogeneous $q = 0.1$ (C300_S_01) model assuming various values of η . Individual curves are marked with the value of η assumed. The thick solid line shows the profile for the $\dot{M} \propto r$ model with no internal absorption for comparison.

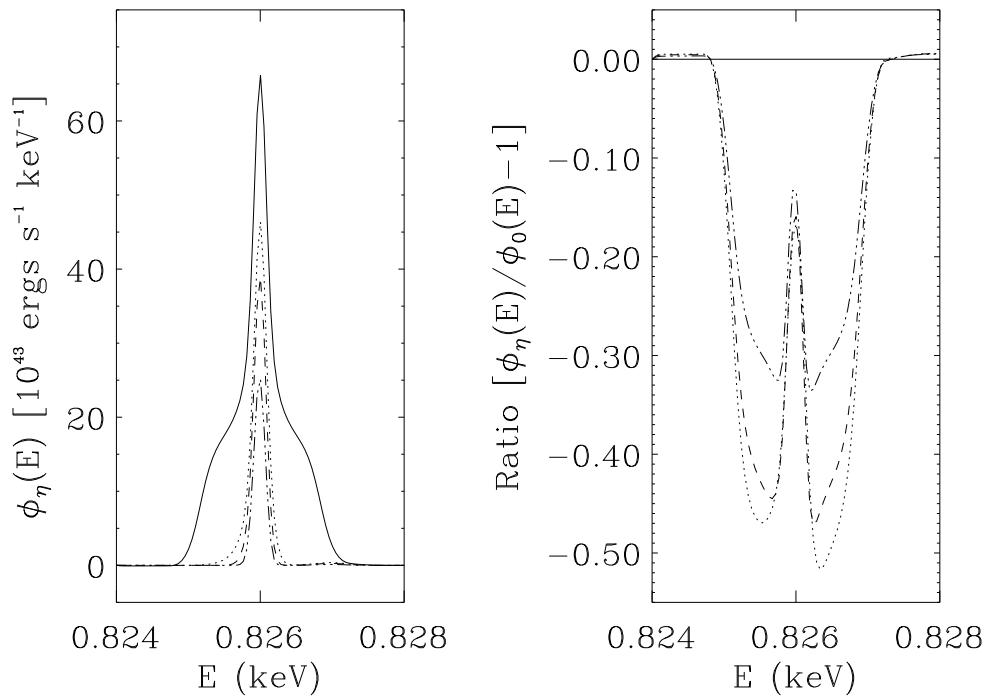


Fig. 9.— The left panel shows the integrated spectral line profile, $\phi_\eta(E)$, for the Fe XVII line at 0.826 keV for different values of the efficiency parameter η . These profiles correspond to a fairly homogeneous $q = 0.1$ (C300_8_01) model, and assume thermal line broadening. The continuum flux has been subtracted from each profile. The right panel shows the ratio of the emergent profiles to the model with no internal absorption. Curves are shown for values of $\eta = 0.0$ (solid line), $\eta = 0.01$ (dotted line), $\eta = 0.1$ (dashed line), and $\eta = 1.0$ (dash-dot-dot-dot line).

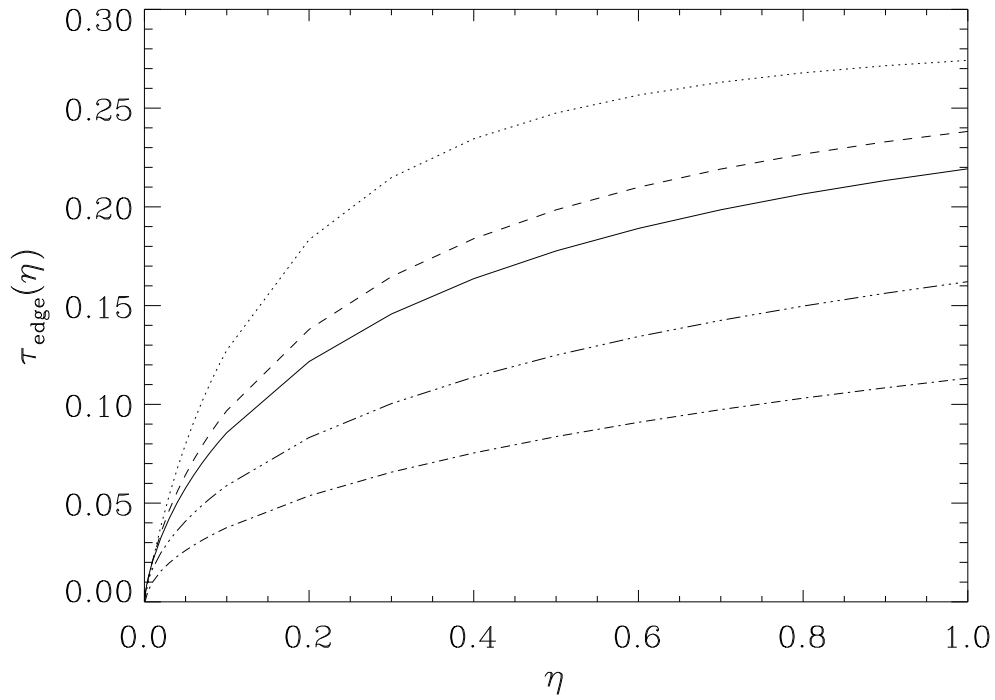


Fig. 10.— The optical depth in the O K edge at 0.532 keV in our models is shown for different values of the deposition efficiency parameter η . No foreground Galactic absorption has been included. Curves are shown for models with $q = 0.1$ (dash-dot line), $q = 0.3$ (dash-dot-dot-dot line), $q = 1.0$ (solid line), $q = 4.0$ (dotted line), and $\dot{M} \propto r$ (dashed line).

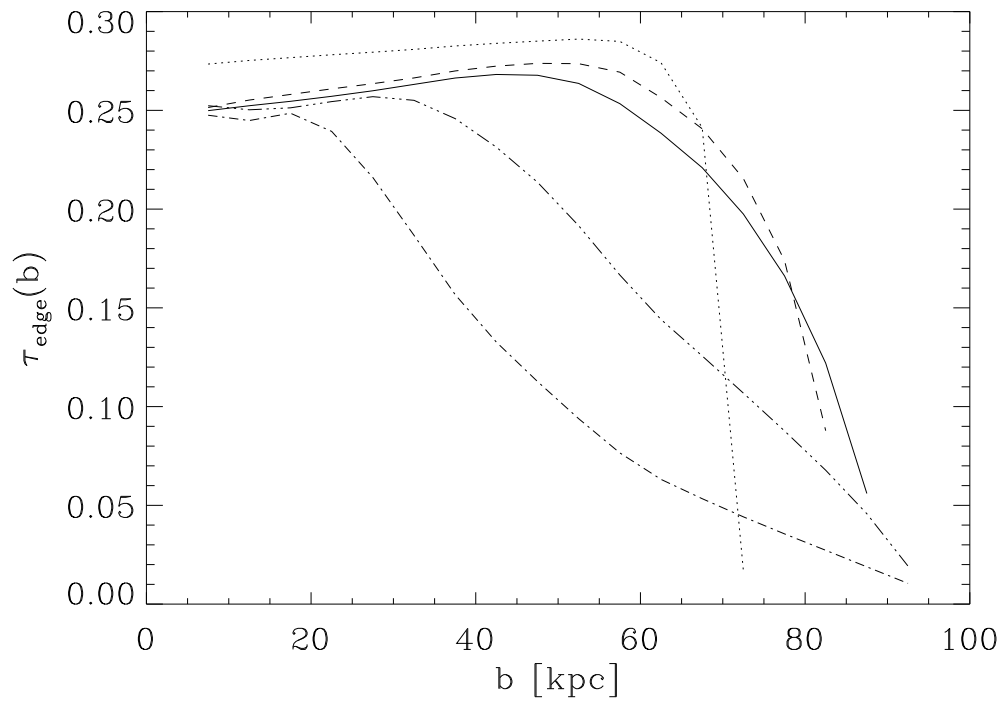


Fig. 11.— The optical depth in the O K edge at 0.532 keV is shown as a function of projected radius for our models. The model spectra were accumulated in 5 kpc annular bins and a value of $\eta = 1$ was assumed. The notation is the same as in Figure 10.

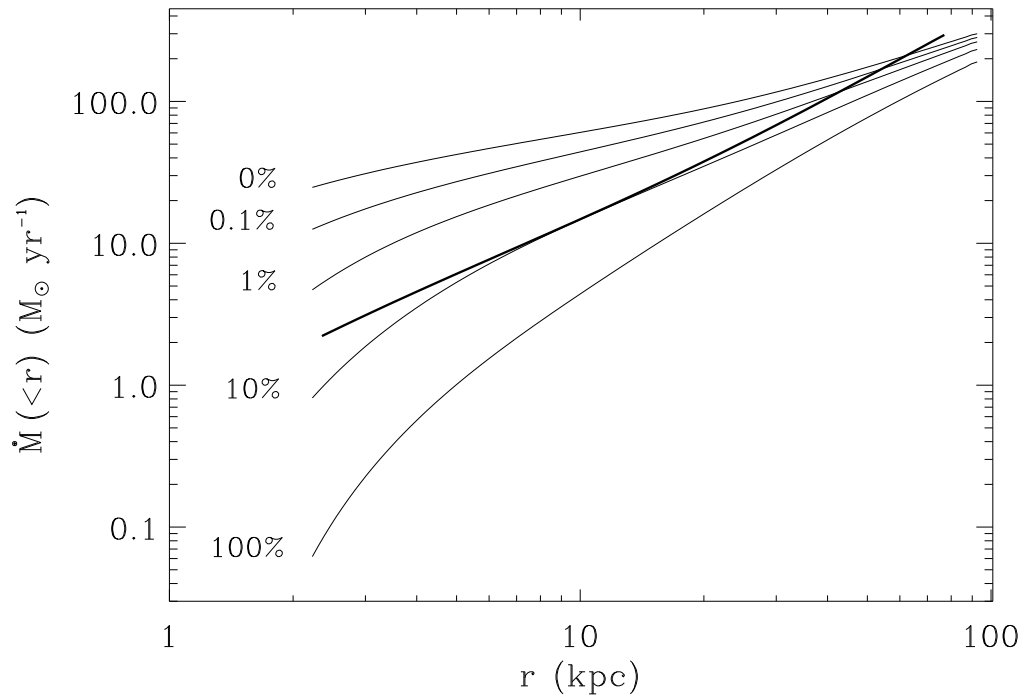


Fig. 12.— The deprojected mass deposition profiles, $\dot{M}(r)$, derived from the *ROSAT* PSPC X-ray surface brightness profiles calculated for the $q = 0.1$ model (C300_8_01) and shown in Figure 5. Each curve is labeled with the corresponding value of η expressed as a percentage. For comparison, the heavy solid line shows the expected mass deposition profile for a model with $\dot{M}(<r) \propto r$.

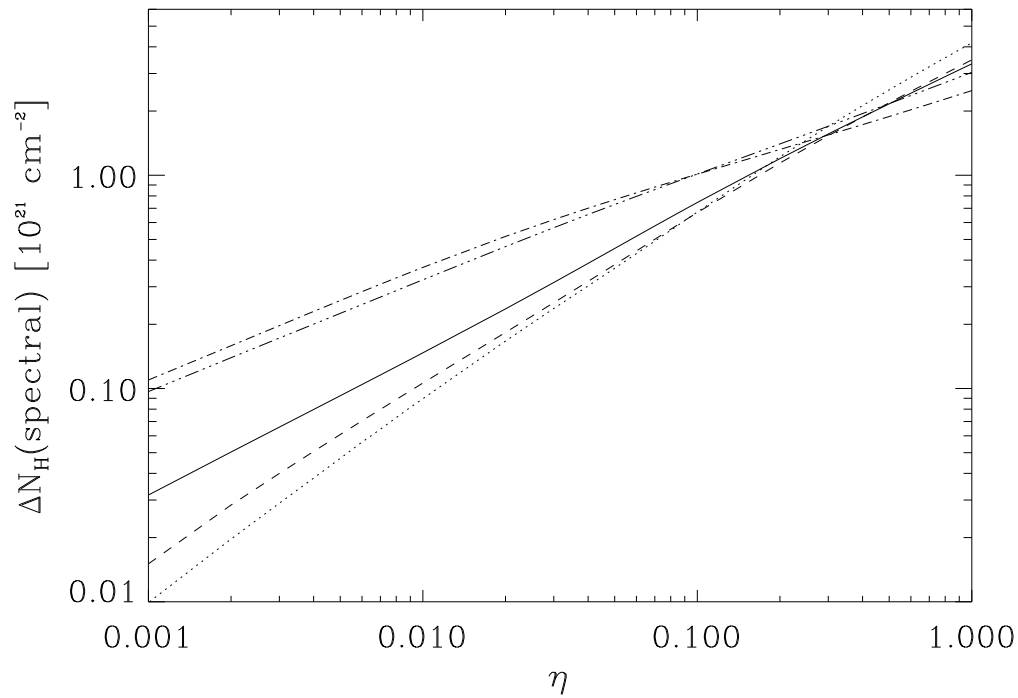


Fig. 13.— The excess absorbing column density for the various models derived from spectral fitting assuming foreground absorption is shown as a function of η . The ordinate values represent the measured excess column after having been folded through the *ROSAT* PSPC response. For all models, a foreground absorbing column of $N_H = 2.0 \times 10^{20} \text{ cm}^{-2}$ was assumed and has been subtracted. All of the models have $\dot{M}_c = 300 M_\odot \text{ yr}^{-1}$ and $T_c = 8 \times 10^7 \text{ K}$. Curves are shown for models with $q = 0.1$ (dash-dot line), $q = 0.3$ (dash-dot-dot-dot line), $q = 1.0$ (solid line), $q = 4.0$ (dotted line), and $\dot{M} \propto r$ (dashed line).

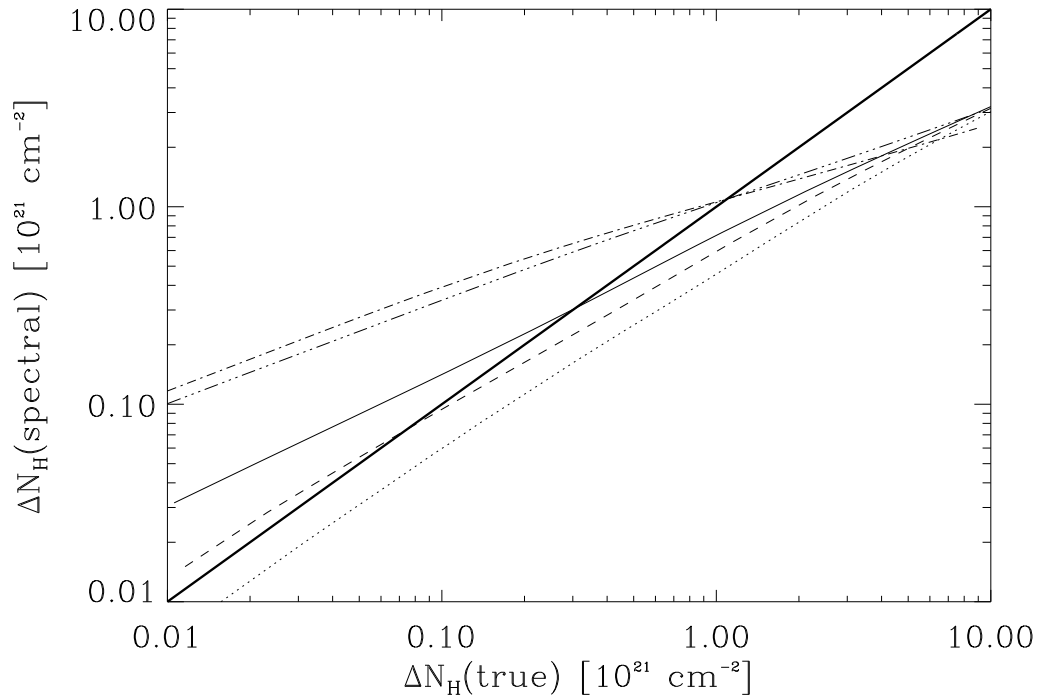


Fig. 14.— A comparison between the actual average internal absorption columns and the values measured from fits to the spectra. The actual average excess column is shown on the abscissa and is given by $\Delta N_H(true) = \dot{M}_c t_a \eta / (1.47 m_p \pi r_c^2)$. The ordinate values are the same spectrally derived columns shown in Figure 13. The models and notation are the same as in that Figure, except that the heavy solid line indicates a one-to-one correspondence between $\Delta N_H(true)$ and $\Delta N_H(spectral)$.

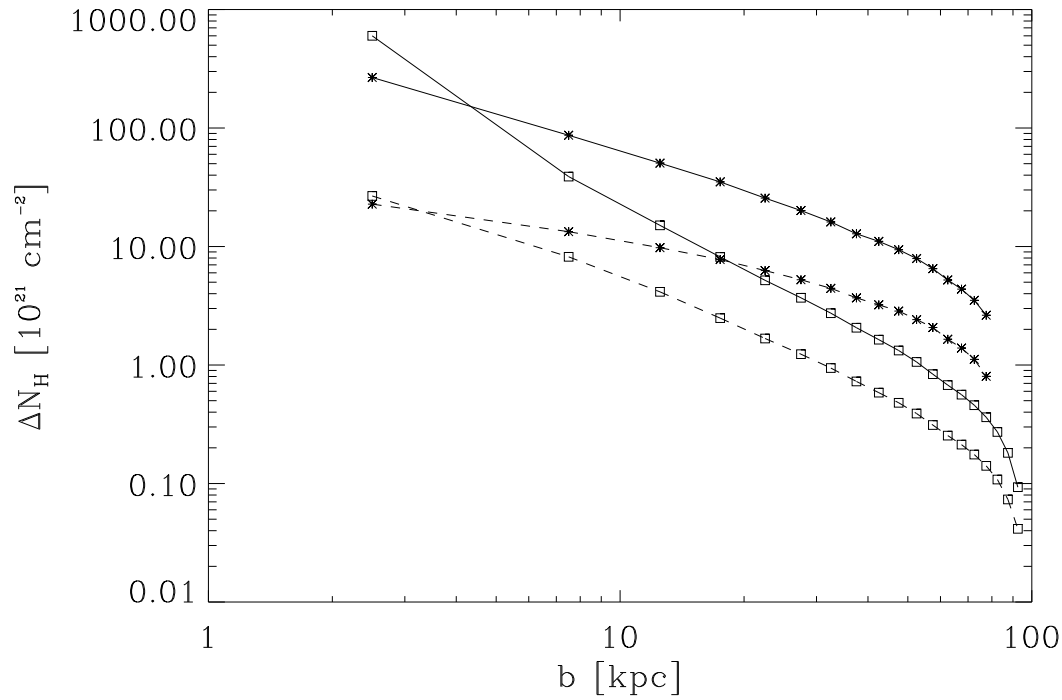


Fig. 15.— The variation in the true average internal absorption column and the fitted column as a function of projected radius for two cooling flow models. The slightly inhomogeneous $q = 0.1$ model (C300_8.01) model is denoted by square symbols while the model with $\dot{M}(r) \propto r$ (C300_8_fb) is denoted by the stars. The model spectra were accumulated in 5 kpc annular bins and fit with a foreground absorption model as in Figures 13 and 14. A value of $\eta = 1$ was used in both cases. For a given model, the solid line shows the true average column in the bin and the dashed line shows the resulting fitted values. A foreground absorbing column of $N_H = 2.0 \times 10^{20} \text{ cm}^{-2}$ was assumed and has been subtracted.